NANOTECHNOLOGY CHARACTERIZATION LABORATORY

Prepared for Dendritic Nanotechnologies, Inc.

Dendrimer-Based MRI Contrast Agents

December 2006

NCL200612A

Nanotechnology Characterization Laboratory

National Cancer Institute at Frederick
SAIC-Frederick, Inc.
Frederick, MD 21702
(301) 846-6939 • ncl@ncifcrf.gov
http://ncl.cancer.gov

TABLE OF CONTENTS

EXECUTIVE SUMMARY

The objective of the Dendritic Nanotechnologies, Inc. - NCL collaboration is to characterize a PAMAM dendrimer with an associated gadolinium chelate MRI contrast agent. The nanomaterials submitted for testing at the NCL were (NCL20) G4 tris (hydroxyl) terminated PAMAM dendrimer, (NCL21) G4 pyrrolidinone terminated PAMAM dendrimer, (NCL22) G4.5 COONa terminated PAMAM dendrimer, (NCL23) G4.5 COONa terminated PAMAM dendrimer-Magnevist® complex, (NCL25) G4 tris (hydroxyl) terminated PAMAM dendrimer-Magnevist® complex, and (NCL26) G4 pyrrolidinone terminated PAMAM dendrimer-Magnevist® complex. Commercially available Magnevist® (NCL24) was used as a control. NCL studies addressed in this report can be divided into three main categories: physicochemical characterization; immunotoxicology; in vitro toxicology.

Physicochemical Characterization

Dynamic light scattering (DLS) technique was used to measure the hydrodynamic size of this dendritic nanomaterial. The effects of sample concentration, buffer, and temperature on the hydrodynamic size (stability) also were measured. Purity was analyzed by HPLC and Capillary Electrophoresis. MALDI-TOF Mass spectrometry was used to obtain the molecular weight information and to determine the purity, existence of dimers, trimers, and trailing generations in the sample. Gadolinium quantitation, which is important to determine the relaxivity as a MRI contrast agent, was carried out by Inductively Coupled Plasma Optical Emission Spectroscopy (ICP-OES). Fractionation methods such as Size Exclusion Chromatography (SEC) and Asymmetric-flow Field Flow Fractionation (AFFF) were used to determine the molecular weight information as well as purity. Finally, a 3T clinical MRI machine was used to obtain relaxivity measurements on this sample to compare with free Magnevist®. No significant relaxivity change was observed upon association of Magnevist® with the dendrimer.

Immunotoxicology

Evaluation of nanoparticle blood contact properties included study of the effects on coagulation pathways and the integrity of blood cellular components. NCL22, NCL23 and NCL24 were free of hemolytic and platelet aggregation effects, though a mild increase in collagen-induced platelet aggregation was noted at high NCL23 and NCL24 concentrations.

Important findings included potential interference of NCL22, NCL23 and NCL24 with plasma coagulation factors, and complement activation by NCL23 and NCL24. Particle effects on in vitro immune function were also evaluated. NCL22, NCL23 and NCL24 were not internalized via phagocytic uptake, and did not alter leukocyte proliferation, macrophage oxidative burst or macrophage chemotaxis. None of the test materials were capable of inducing cytokines in human peripheral blood mononuclear cells, and minimal effects on natural killer cell activity were observed. Of potential clinical relevance, NCL23

and NCL24 were found to have mild myelosuppressive properties, and NCL23 and NCL24 inhibited macrophage phagocytic activity. These properties appear to be associated with the Magnevist® (NCL24) component of the nanotech strategy.

In Vitro Toxicology

Nanoparticle biocompatibility was evaluated in porcine renal proximal tubule and human hepatocarcinoma cell lines. NCL22, NCL23 and NCL24 were found to be minimally cytotoxic to these cells lines, under the experimental conditions utilized. Further in vitro mechanistic toxicology studies were not warranted at this time.

In summary, in vitro evaluation of the dendrimer-Magnevist® complex demonstrated a high degree of biocompatibility, with minimal negative effects on cell viability, immune function and blood components. Future studies will examine the in vivo tumor imaging capabilities of the contrast agents in animal models.

NANOPARTICLE DESCRIPTIONS

All dendrimers have a diaminobutane (DAB) core and polyamidoamine (PAMAM) branching with different terminal functional groups. The samples that were submitted by DNT are:

NCL20: G4 Tris(hydroxy) terminated dendrimer. The theoretical number of terminal Tris groups is 64. The theoretical molecular weight is 18.15 kDa.

NCL21: G4 Pyrrolidinone terminated dendrimer. The theoretical number of terminal pyrrolidinone groups is 64. The theoretical molecular weight is 22.31 kDa.

NCL22: Generation 4.5 (G4.5) COONa terminated dendrimer. The theoretical number of terminal carboxylic groups is 128. The theoretical molecular weight is 26.28 kDa.

NCL23 is NCL22 with associated Magnevist® in a dendrimer-Magnevist® complex.

NCL24 is free Magnevist®.

NCL25 is NCL20 with associated Magnevist® in a dendrimer-Magnevist® complex.

NCL26 is NCL21 with associated Magnevist® in a dendrimer-Magnevist® complex.

The lead sample compound is NCL23, and the corresponding control is NCL22. Most data generated are based on these two samples.

G4.5 PAMAM Dendrimer (NCL22)

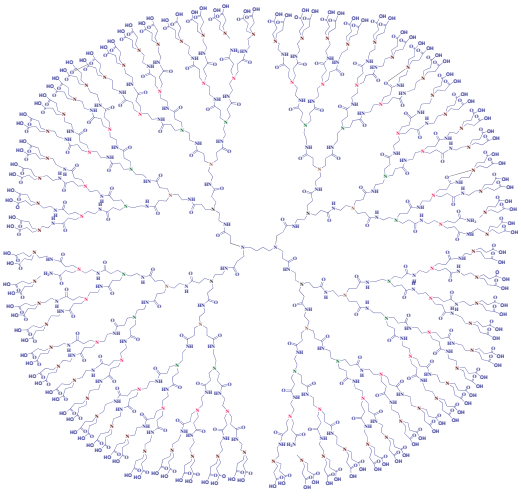

Surface Groups

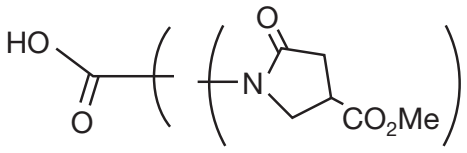

Carboxy Pyrrolidone

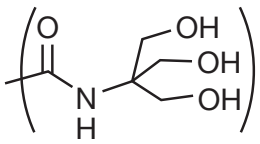

Tris

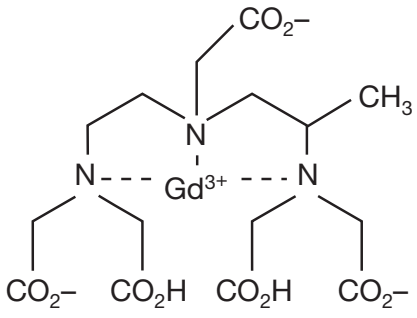

Magnevist

PHYSICAL CHEMICAL CHARACTERIZATION

SECTION SUMMARY

The 'lead compound' of this project, as proposed by DNT, is a generation 4.5 (Carboxy terminated) PAMAM dendrimer (NCL23) in a dendrimer-Magnevist® complex. Extensive physical characterization was carried out on this sample along with the corresponding control dendrimer not associated with Magnevist® (NCL22). Dynamic light scattering (DLS) technique was used to measure the hydrodynamic size of this dendritic nanomaterial. The effects of sample concentration, buffer, and temperature on the hydrodynamic size (stability) were also measured. Purity was analyzed by HPLC and Capillary Electrophoresis. MALDI-TOF Mass spectrometry was used to obtain the molecular weight information and to determine the purity, existence of dimers, trimers, and trailing generations in the sample. Gadolinium quantitation, which is important to determine the relaxivity as a MRI contrast agent, was carried out by Inductively Coupled Plasma Optical Emission Spectroscopy (ICP-OES). Fractionation methods such as Size Exclusion Chromatography (SEC) and Asymmetric flow Field Flow Fractionation (AFFF) were used to determine the molecular weight information as well as purity. Finally, a 3T clinical MRI machine was used to obtain relaxivity measurements on this sample to compare with free Magnevist®. No significant relaxivity change was observed upon association of the dendrimer with Magnevist®.

Hydrodynamic Size/Size Distribution via Dynamic Light Scattering (DLS)

Hydrodynamic Size versus Solvent and Temperature

NCL-##	Temperature (°C)	Media	Z-avg (nm)	PdI	Peak (nm)
22	25	Saline	8.5	0.200	6.0
22	25	PBS	6.6	0.214	5.2
22	37	PBS	7.9	0.282	5.1
23	25	Saline	7.4	0.235	5.3
23	25	PBS	8.4	0.265	6.1
23	37	PBS	9.8	0.358	5.6
20	25	Saline	5.2	0.122	4.4
20	25	PBS	8.6	0.211	6.2

Table 1. Summary of the effect of solvent and temperature on the hydrodynamic size for NCL22, NCL23 and NCL20. Hydrodynamic size (diameter) of the dendrimer samples NCL22, NCL23 and NCL20 were measured in aqueous solutions using DLS at 25 °C and 37 °C. An instrument with a backscattering detector was used for these measurements in batch mode (no fractionation). This technique does not have the resolving power of differentiating monomers and dimers without fractionation. Samples were weighed, dissolved in deionized (DI) water, aliquoted, lyophilized and resuspended in desired buffer solutions to a final concentration of 1 mg/mL, and filtered through a 0.2-µm filter, unless otherwise indicated. The measurements were taken in saline (154 mM NaCl) and phosphate-buffered saline (PBS) at pH 7.4. Three measurements were taken for each sample. For NCL22, the size is slightly larger when dispersed in saline compared to PBS. In PBS, the size is independent of temperature. This is in contrast to NCL23, which is larger in PBS than in saline. NCL23 also shows temperature dependence, as its size decreases slightly with increased temperature in PBS. Finally, NCL20 is larger when dispersed in PBS compared to saline. For each sample, the intensity weighted mean diameter (Z-avg) derived from the cumulants analysis and the diameter after conversion to volume-weighted distribution are provided on the following pages.

NCL22: 1 mg/mL, saline, 25 °C
Z-avg size = 8.5 nm
PdI = 0.200
Peak = 6.0 nm (100% vol)

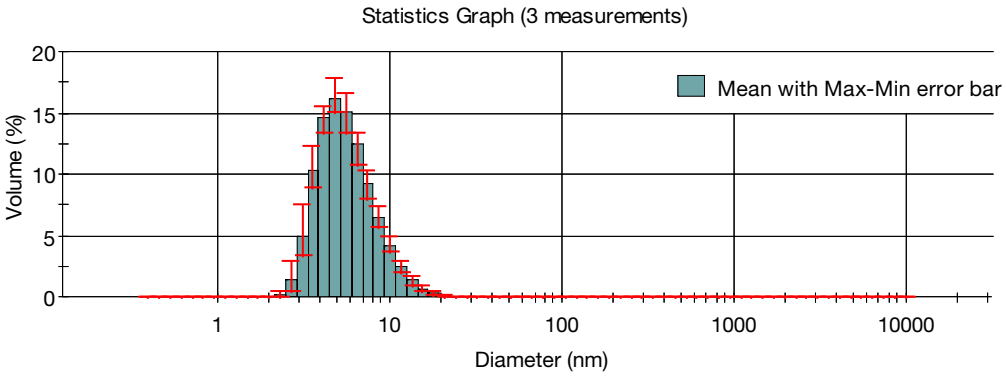

Figure 1. Statistics graph based on size distribution by volume for NCL22 in saline at 25 °C. Results are tabulated in Table 1.

NCL22: 1 mg/mL, PBS, 25 °C
Z-avg = 6.6 nm
PdI = 0.214
Peak = 5.2 nm (100% vol)

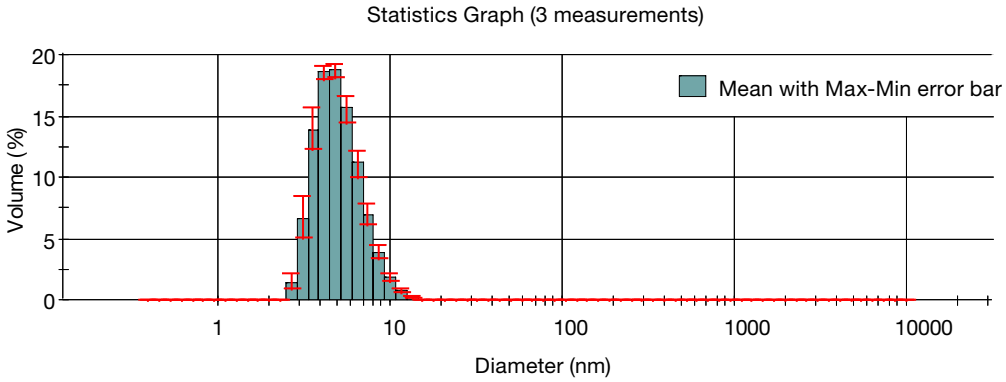

Figure 2. Statistics graph based on size distribution by volume for NCL22 in PBS at 25 °C. Results are tabulated in Table 1.

NCL22: 1 mg/mL, PBS, 37 °C
Z-avg size = 7.9 nm
PdI = 0.282
Peak = 5.1 nm (100% vol)

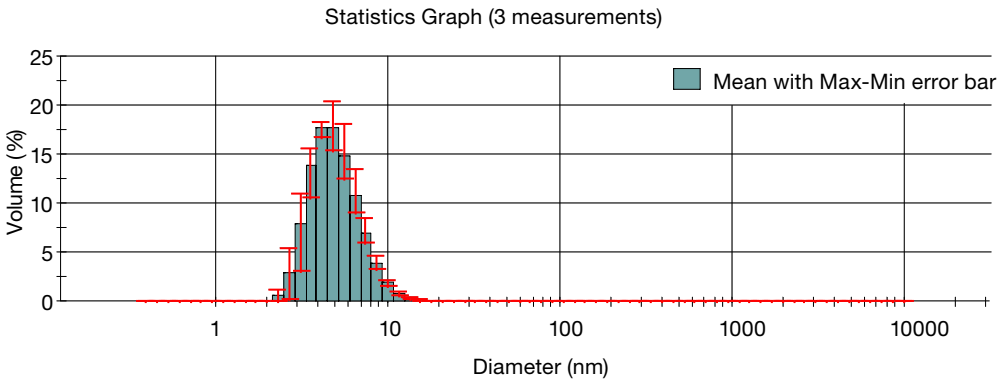

Figure 3. Statistics graph based on size distribution by volume for NCL22 in PBS at 37 °C. Results are tabulated in Table 1.

NCL23: 1 mg/mL, saline, 25 °C
Z-avg = 7.4 nm
PdI = 0.235
Peak = 5.3 nm (100% vol)

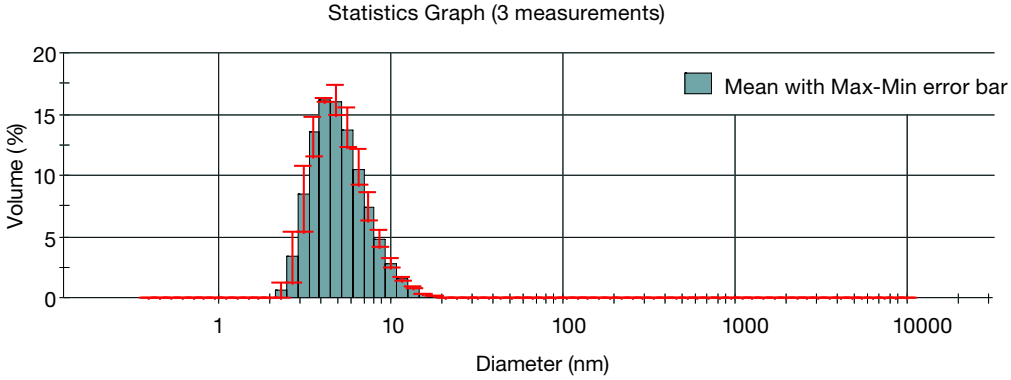

Figure 4. Statistics graph based on size distribution by volume for NCL23 in saline at 25 °C. Results are tabulated in Table 1.

NCL23: 1 mg/mL, PBS, 25 °C
Z-avg size = 8.4 nm
PdI = 0.265
Peak = 6.1 nm (100% vol)

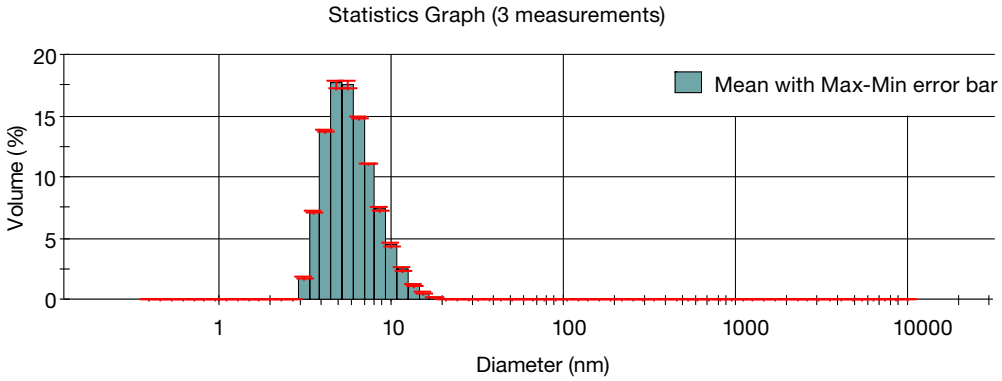

Figure 5. Statistics graph based on size distribution by volume for NCL23 in PBS at 25 °C. Results are tabulated in Table 1.

NCL23: 1 mg/mL, PBS, 37 °C
Z-avg size = 9.8 nm
PdI = 0.358
Peak = 5.6 nm (100% vol)

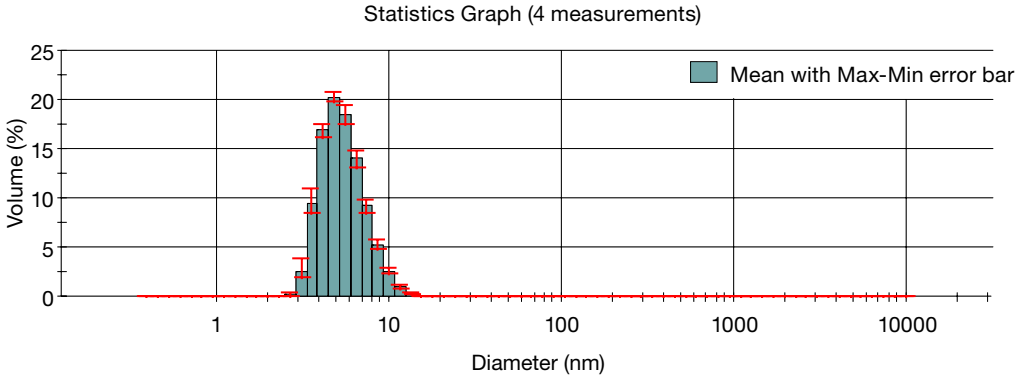

Figure 6. Statistics graph based on size distribution by volume for NCL23 in PBS at 37 °C. Results are tabulated in Table 1.

NCL20: 1 mg/mL, saline, 25 °C
Z-avg size = 5.2 nm
PdI = 0.122
Peak = 4.4 nm (100% vol)

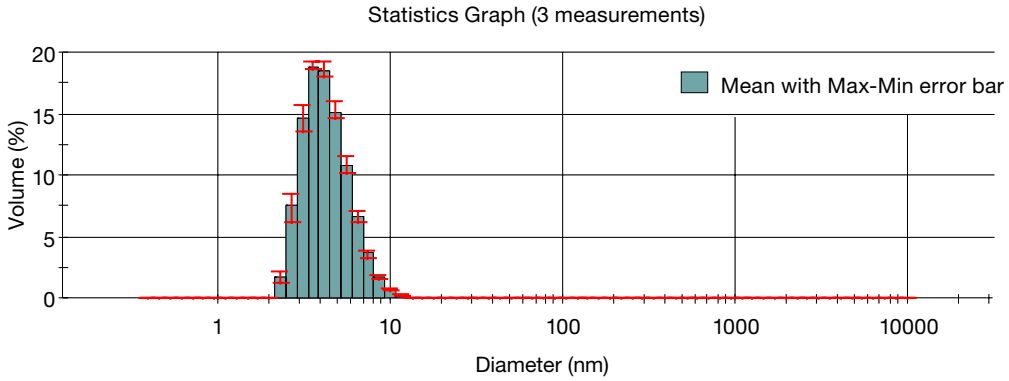

Figure 7. Statistics graph based on size distribution by volume for NCL20 in saline at 25 °C. Results are tabulated in Table 1.

NCL20: 1 mg/mL, PBS, 25 °C
Z-avg size = 8.6 nm
PdI = 0.211
Peak = 6.2 nm (100% vol)

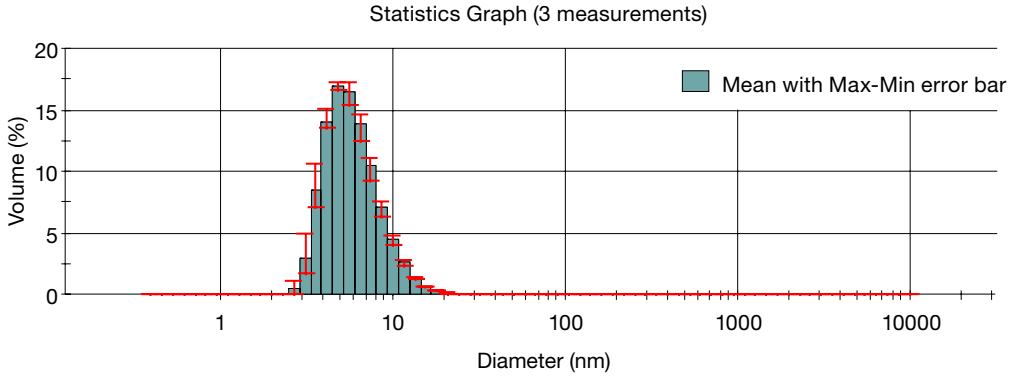

Figure 8. Statistics graph based on size distribution by volume for NCL20 in PBS at 25 °C. Results are tabulated in Table 1.

Thermal Stability of NCL22

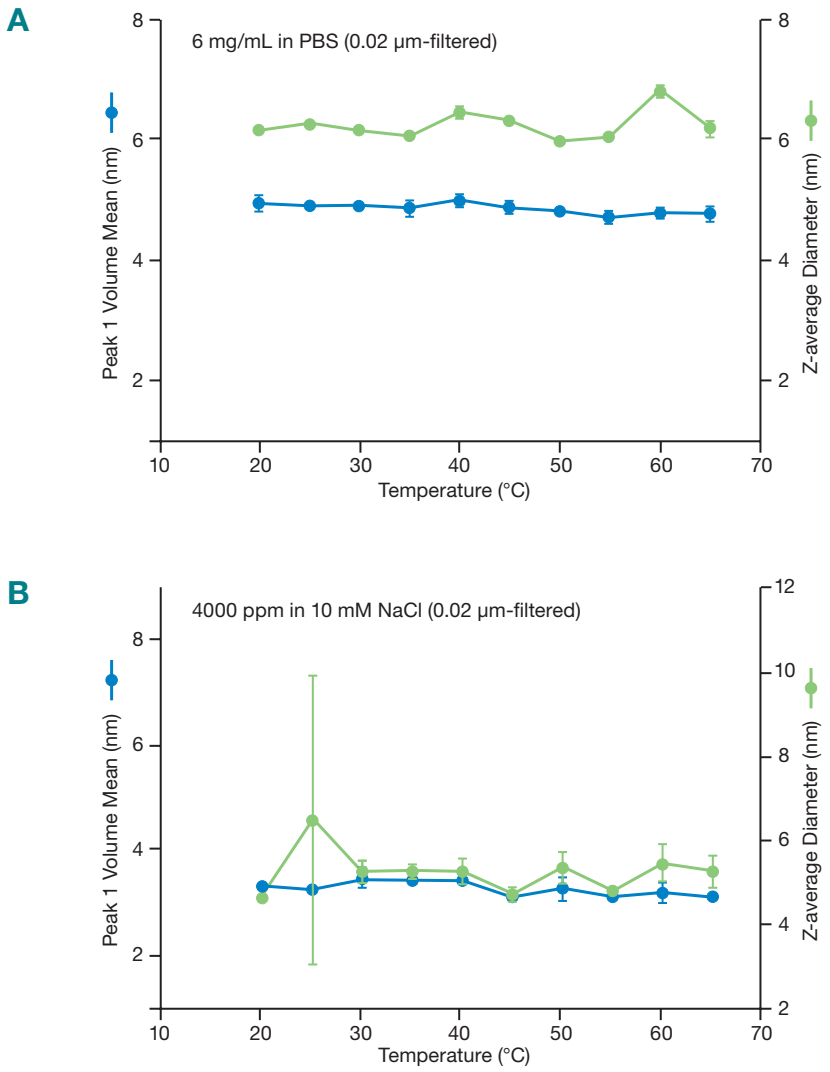

Figure 9. The effect of hydrodynamic size of NCL22 on temperature in PBS (A) and in 10 mM NaCl (B). The thermal stability of NCL22 as measured by DLS was studied over a temperature range of 20–65 °C and in two different solvents. Samples were 6 mg/mL in PBS and 4 mg/mL (4000 ppm) in 10 mM NaCl and were filtered through a 0.02-µm filter. The results are shown above and indicate no temperature dependence on the size (labeled "peak 1 vol mean (nm)" in graphs) in either solvent. The huge error bar for the 25 °C data point in Figure 9, B, is due to an aberration data point in the measurements.

Hydrodynamic Size Comparison of NCL22 and NCL23

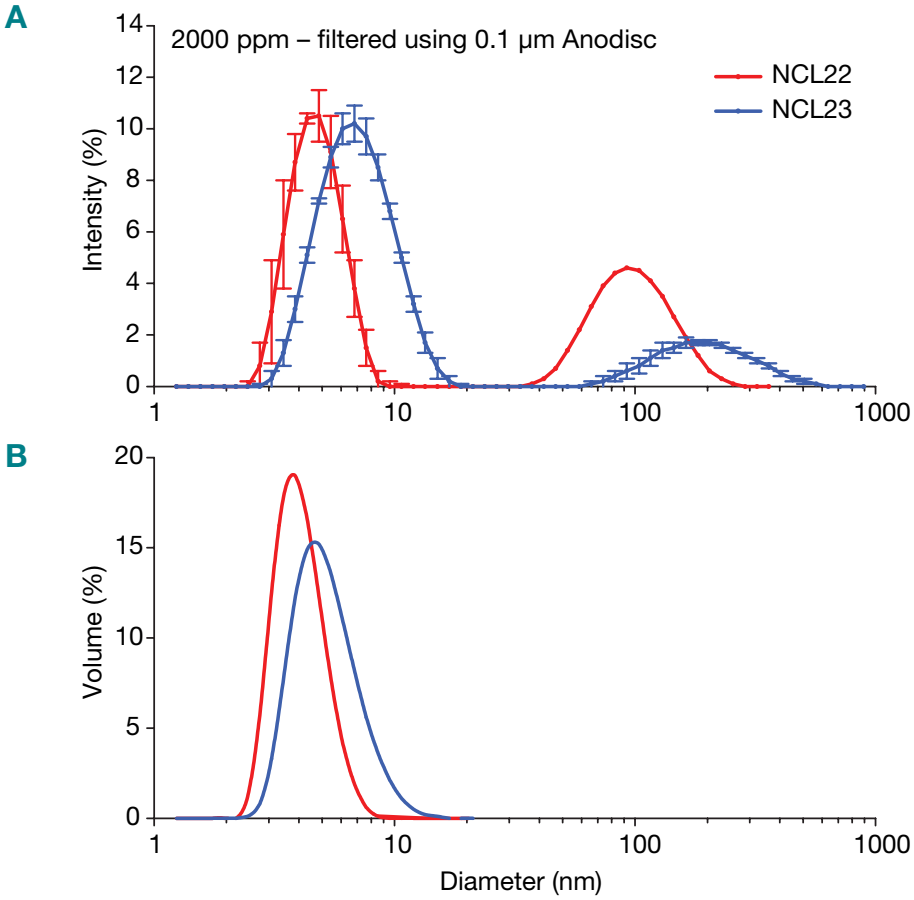

Figure 10. The intensity-weighted (A) and volume-weighted size distribution (B) plots for NCL22 and NCL23. Multiple DLS measurements of NCL22 and NCL23 at 2000 ppm (2 mg/mL) in 10 mM NaCl were averaged and presented as intensity (Figure 10, A) and volume (Figure 10, B) distributions calculated using a non-negative least squares (NNLS) fit to the inverse Laplace transform. Limited data suggest a slight increase in size occurs because of the presence of Gd-complex, but more extensive data are needed to confirm this suggestion. For particles in the sub-100 nm range, the scattered intensity exhibits a d^6 dependence, where d is the diameter. In other words, a single 100-nm particle will scatter roughly the same amount of light as 1,000,000 particles with a diameter of 1 nm. That is why the conversion to volume from intensity indicates that the smaller mode is predominant on a volume (or number) basis, and the larger mode virtually disappears. The smaller particle size peak below 10 nm is identified as the “primary” size.

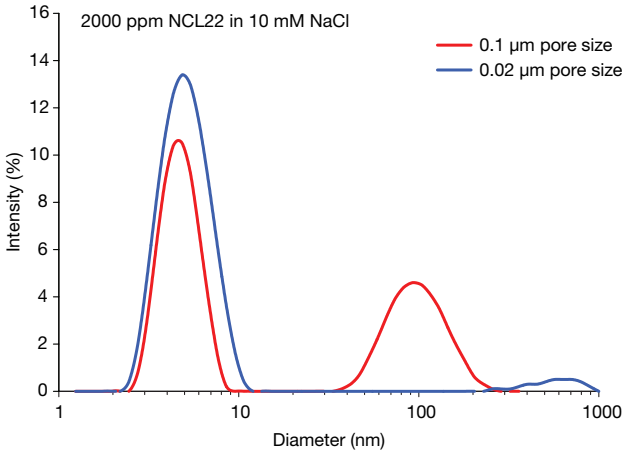

Figure 11. The effect of prefiltration on hydrodynamic size of NCL22 in 10 mM NaCl. Using a 0.1-µm-pore-size filter during sample preparation consistently results in the appearance of a size mode near 100 nm in the intensity distribution derived from DLS measurements on NCL22 and NCL23 dendrimer samples. Using a 0.02-µm-pore-size filter causes the large-size mode to be removed, indicating that this is a real mode and not an analysis artifact. Additional measurements on DI water and saline solution filtered in the same manner, but not containing the dendrimer sample, did not indicate presence of a large-size mode with similar intensity. The origin of peak has not been resolved, but it may result from large dendrimer agglomerates that either exist in the sample after redispersion, or that are formed during the filtration process itself. The technique cannot resolve the presence of dimers and trimers.

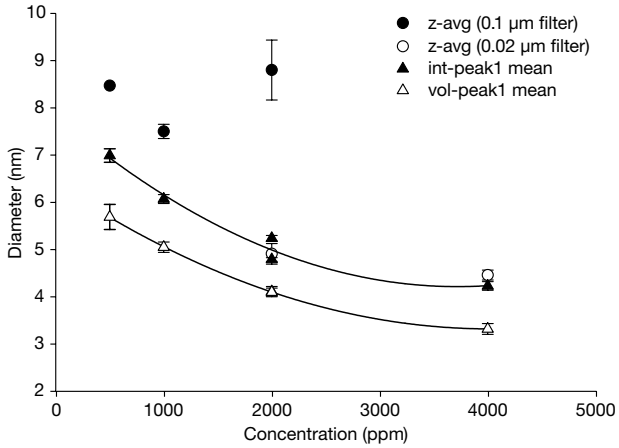

Figure 12. The effect of concentration of NCL22 on hydrodynamic size in 10 mM NaCl. DLS batch measurements on NCL22 in 10 mM NaCl indicate a dependence for the hydrodynamic diameter on dendrimer concentration, approaching a flat region at concentrations above 2000 ppm (2mg/mL). The Z-average diameter remains fairly high and subject to large variation across measurements when the sample is prefiltered using a 0.1-µm-pore-size alumina membrane. In the absence of prefiltering, data are too noisy for analysis. However, prefiltration with a 0.02-µm filter results in a Z-average that is close to the calculated primary peak diameter from a NNLS analysis of the correlation data. The primary peak size (indicated as “peak1” in the graph) is independent of the presence or absence of larger-size peaks. Conversion of the intensity distribution to a volume basis using the Rayleigh-Debye-Gans (RDG) optical model assumption (no dependence on refractive index of particles) yields a slightly smaller mean peak diameter for the primary peak. Clearly, particle concentration and sample preparation can affect the DLS results.

Effect of Hydrodynamic Size on NCL23 Concentration in PBS

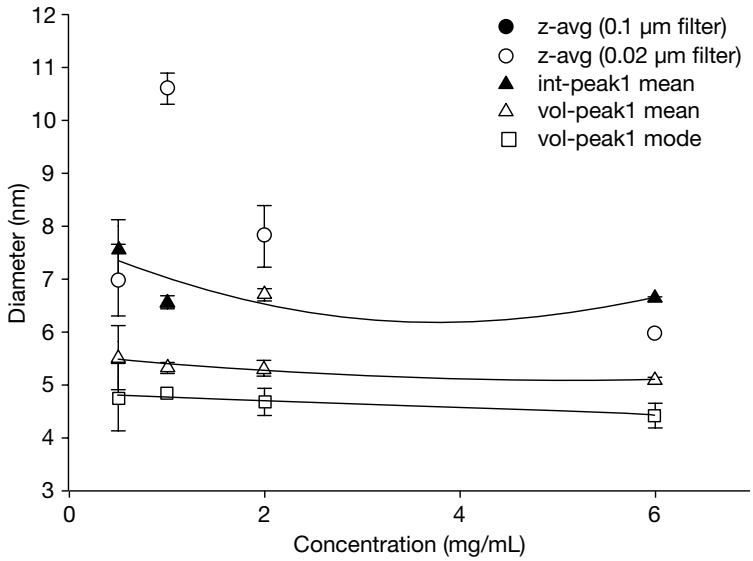

Figure 13. The effect of hydrodynamic size on NCL23 concentration in PBS. DLS batch measurements on NCL23 in PBS indicate no dependence on dendrimer concentration for the hydrodynamic diameter (indicated as “peak1” in graph). The Z-average remains fairly high and subject to large variation across measurements when the sample is prefiltered using a 0.1- or 0.02-µm-pore-size alumina membrane.

Particle Number Density and Mean Inter-particle Distance

At 6 mg/mL	
1.6424 E17 den/mL	r_NCL-22 = 11.33 nm
7.9686 E16 den/mL	r_NCL-23 = 14.42 nm
At 0.5 mg/mL	
1.3687 E16 den/mL	r_NCL-22 = 25.93 nm
6.6405 E15 den/mL	r_NCL-23 = 33.00 nm
Calculated double layer thicknesses (Debye layer) at 25 °C	
For 10 mM NaCl, 3.04 nm	
For 154 mM NaCl (isotonic), 0.78 nm	
For PBS (Ionic strength= 0.174), 0.73 nm	

Table 2. Particle Number Density and Mean Inter-particle Distance. For a 5-nm NCL22 dendrimer at 6 mg/mL in 10 mM NaCl, the effective mean separation distance between particles is equal to the r-value minus 5 nm minus 6 nm (3.04 x 2) = approximately 0.3 nm, or less than one particle diameter. In other words, the particles are highly crowded and will be sensing the presence of nearest neighbors. This may affect a change in the actual size (e.g., compaction or shrinkage), or it may result in retarded motion (change in time scale of random motion). Either situation would cause the measured DLS size to vary. At 0.5 mg/mL, the particles are well separated, even taking into consideration the electrical double layer; they are separated by about 3 or 4 particle diameters.

Gadolinium Quantitation via Inductively Coupled Plasma Optical Emission Spectroscopy (ICP-OES)

Per the sample information provided by DNT, NCL23 contains 12.1 wt% Gadolinium (Gd).

Data from ICP-OES analysis:

NCL23 Gd mass fraction (%): 12.9%

Sample preparation: Samples were digested in 1 mL conc. HNO_3 and diluted to a final mass of 20 g. Aliquots of 1-mL were taken from these stocks, diluted to 40 g and then analyzed using an external calibration as an internal standard.

Molecular Weight Measurement by Mass Spectrometry

A

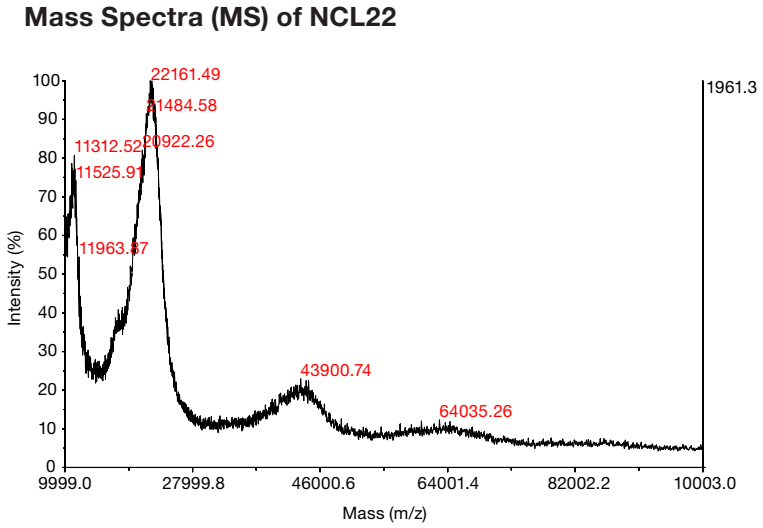

B

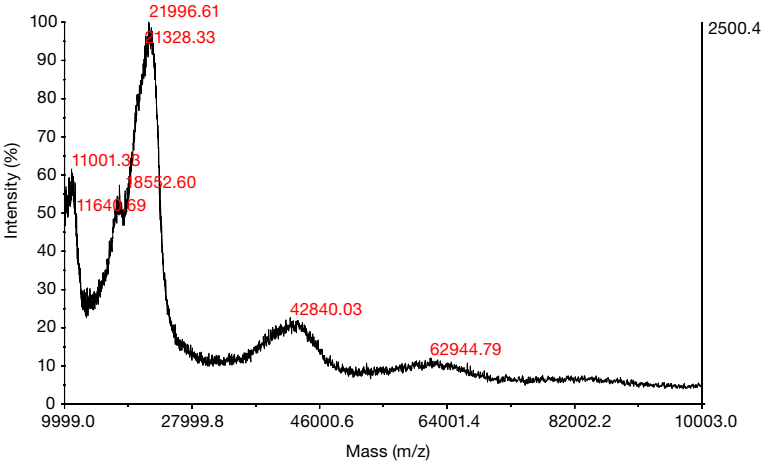

Figure 14. Mass spectra for (A) NCL22 and (B) NCL23. The theoretical molecular weight of NCL22 is 26.28 kDa. The actual/experimental result based on MS was 22 kDa for both samples. The experimental details are as follows: DHB matrix, 10 mg/mL. CH_3CN/H_2O = 3/7 (v/v). Molecular weight spectra obtained by MALDI-TOF, with a major peak at 22 kDa and minor peaks centered around 43 kDa and 64 kDa, are consistent with the information provided by DNT for G4.5 COONa dendrimer samples NCL22 and NCL23. Association with Magnevist did not change the spectrum of NCL23.

UV-Vis Spectra

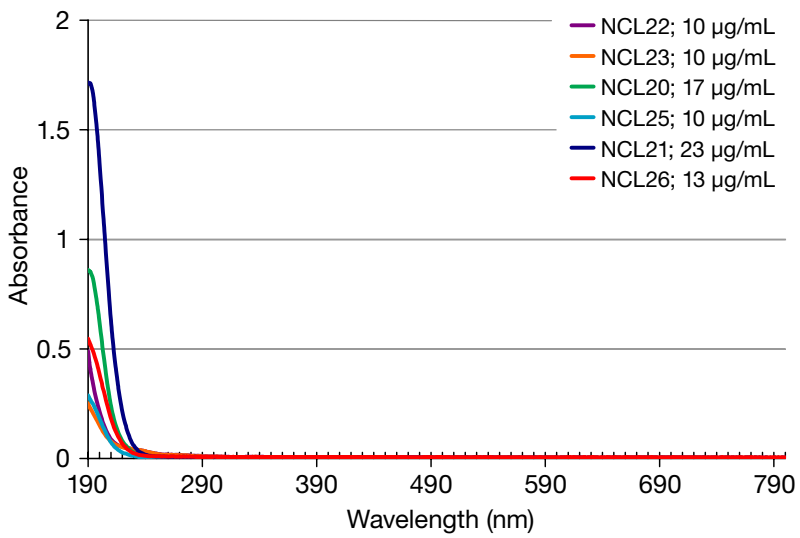

Figure 15. UV-Vis spectra for the dendrimers studied. UV-Vis spectra were recorded using a Thermo Electron Evolution 300 spectrophotometer (Waltham, MA). Samples were prepared in HPLC-grade water and measured in quartz microcuvettes (b = 10 mm, QS109.004, Hellma, Plainview, NY). The UV-Vis spectra are consistent with the dendrimers in that no absorption above 230 nm was observed.

Reverse Phase HPLC

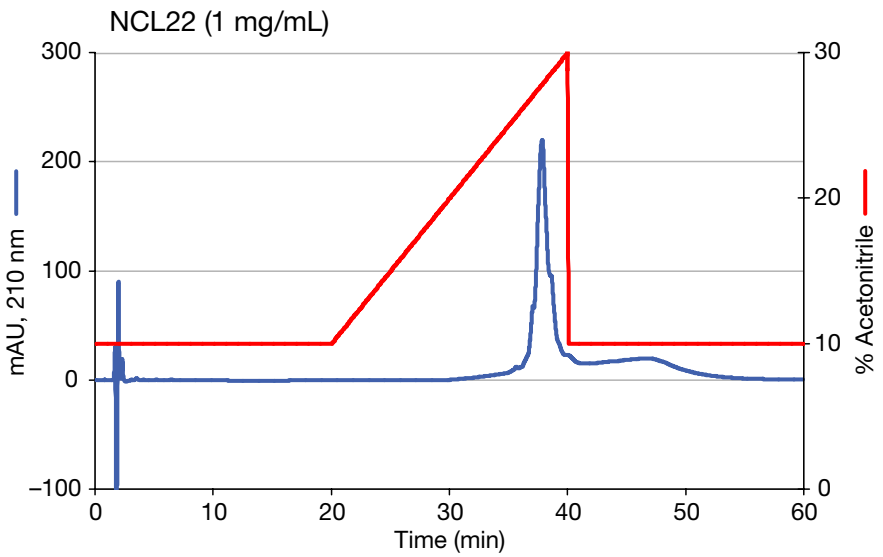

Figure 16. HPLC Chromatogram for NCL22. Reversed-phase high-performance liquid chromatography (RP-HPLC) is a separation technique used for determining the purity of a sample. It is based on the partitioning of the sample molecules with the mobile phase and the stationary, hydrophobic phase. The chromatographic system consisted of a degasser (Agilent G1379A, Palo Alto, CA), capillary pump (Agilent G1378A), micro well-plate autosampler (Agilent G1377A), Zorbax 300SB-C18 column (1.0 mm ID x 150 mm, 3.5 µm, Agilent), and a diode array detector (Agilent G1315B). The mobile phase consisted of water/acetonitrile (HPLC-grade, 0.14 % [w/v] trifluoroacetic acid) at varying volume percentages at a flow rate of 50 µL/min. The elution gradient for each sample is shown in red on the chromatograms. The sample volume injected was 5 µL, typically at a concentration of 1 mg/mL in HPLC water, and the eluted sample was detected at 210 nm. Samples were run in triplicate. The chromatogram and elution profile for NCL22 are shown. The retention time for the main peak is 37.9 min and corresponds to 85% ± 2% of the total area (based on peaks eluted between 36.7 and 39.7 min). The UV spectra (data not shown) for these peaks are consistent with that of NCL22 measured with a UV-Vis spectrophotometer. The nature of the broad peak at 47.2 min is unknown.

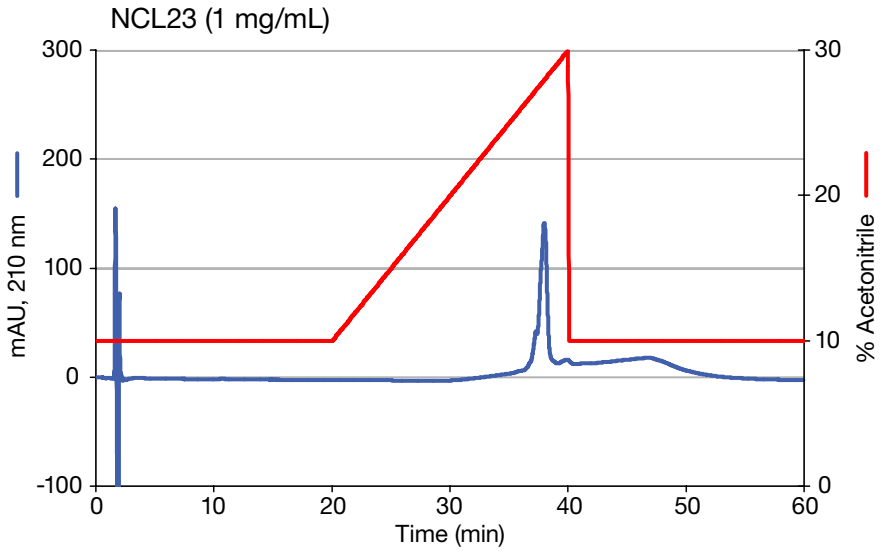

Figure 17. HPLC chromatogram for NCL23. The chromatogram and elution profile for NCL23 are shown. The retention time for the main peak is 38.0 min and corresponds to 79% ± 1% of the total area (based on peaks eluted between 36.9 and 39.9 min). The UV spectra (data not shown) for these peaks are consistent with that of NCL23 measured with a UV-Vis spectrophotometer. The nature of the broad peak at 47.1 min is unknown.

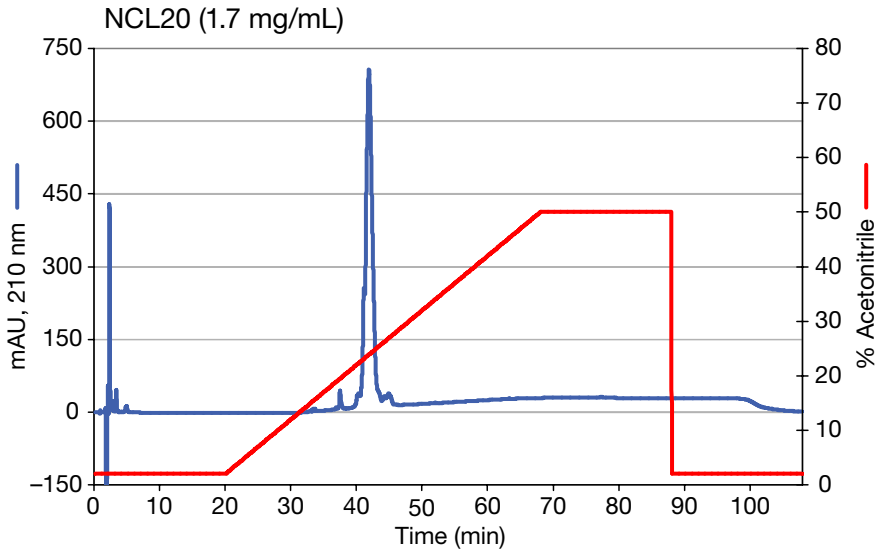

Figure 18. HPLC chromatogram for NCL20. The chromatogram and elution profile for NCL20 are shown. The retention time for the main peak is 41.9 min. The UV spectra (data not shown) for these peaks (eluted between 37.5 and 44.9 min) are consistent with that of NCL20 measured with a UV-Vis spectrophotometer.

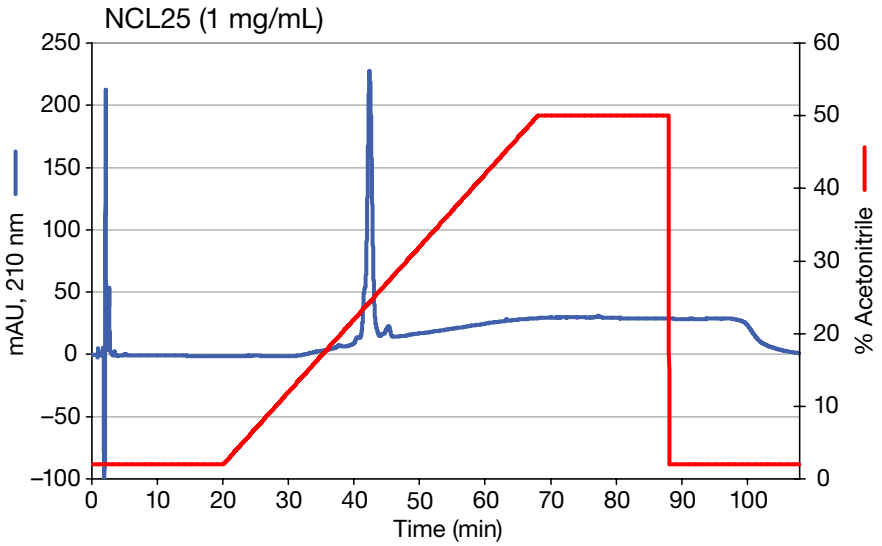

Figure 19. HPLC chromatogram for NCL25. The chromatogram and elution profile for NCL25 are shown. The retention time for the main peak is 42.4 min. The UV spectra (data not shown) for these peaks (eluted between 40.6 and 45.3 min) are consistent with that of NCL25 measured with a UV-Vis spectrophotometer.

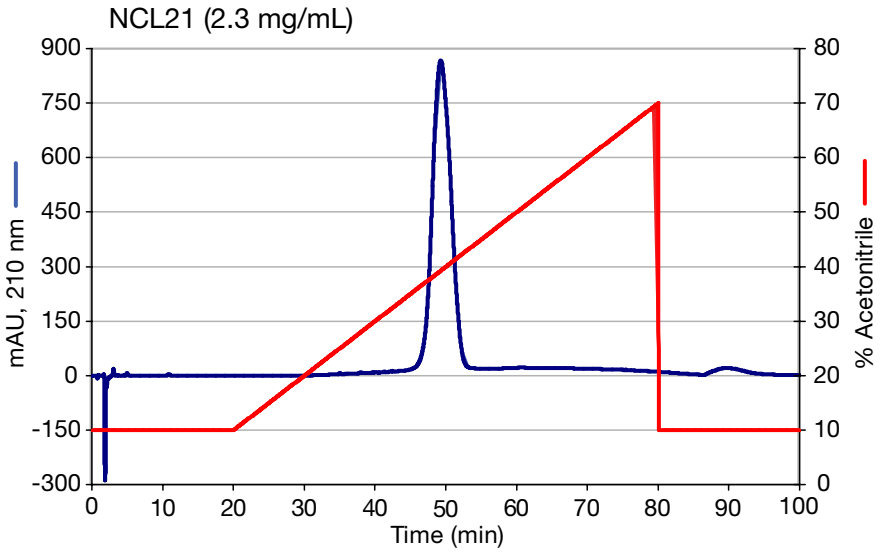

Figure 20. HPLC chromatogram for NCL21. The chromatogram and elution profile for NCL21 are shown. The retention time for the main peak is 49.3 min and corresponds to 96% ± 1% of the total area. The UV spectra (data not shown) for this peak are consistent with that of NCL21 measured with a UV-Vis spectrophotometer. The nature of the broad peak at 89.6 min is unknown.

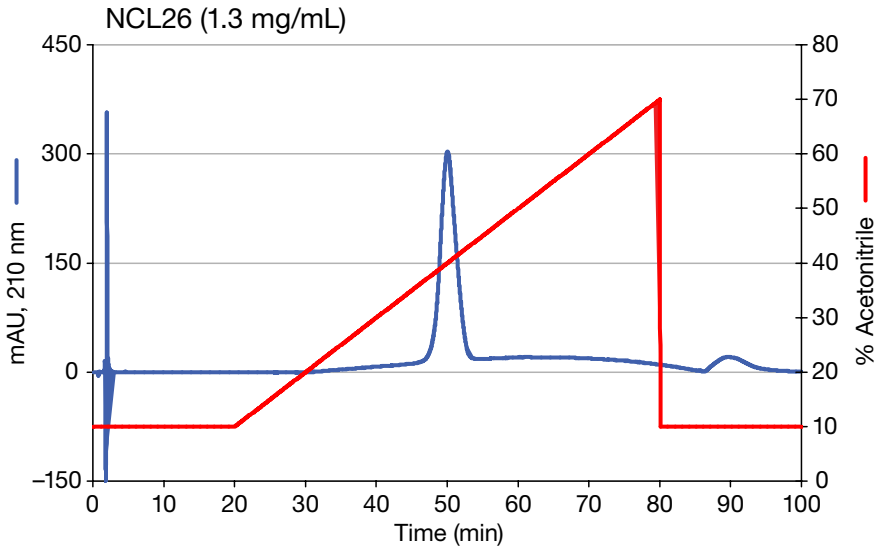

Figure 21. HPLC chromatogram for NCL26. The chromatogram and elution profile for NCL26 are shown. The retention time for the main peak is 50.1 min and corresponds to 88% ± 1% of the total area. The UV spectra (data not shown) for this peak are consistent with that of NCL26 measured with a UV-Vis spectrophotometer. The nature of the broad peak at 89.6 min is unknown.

Capillary Electrophoresis (CE)

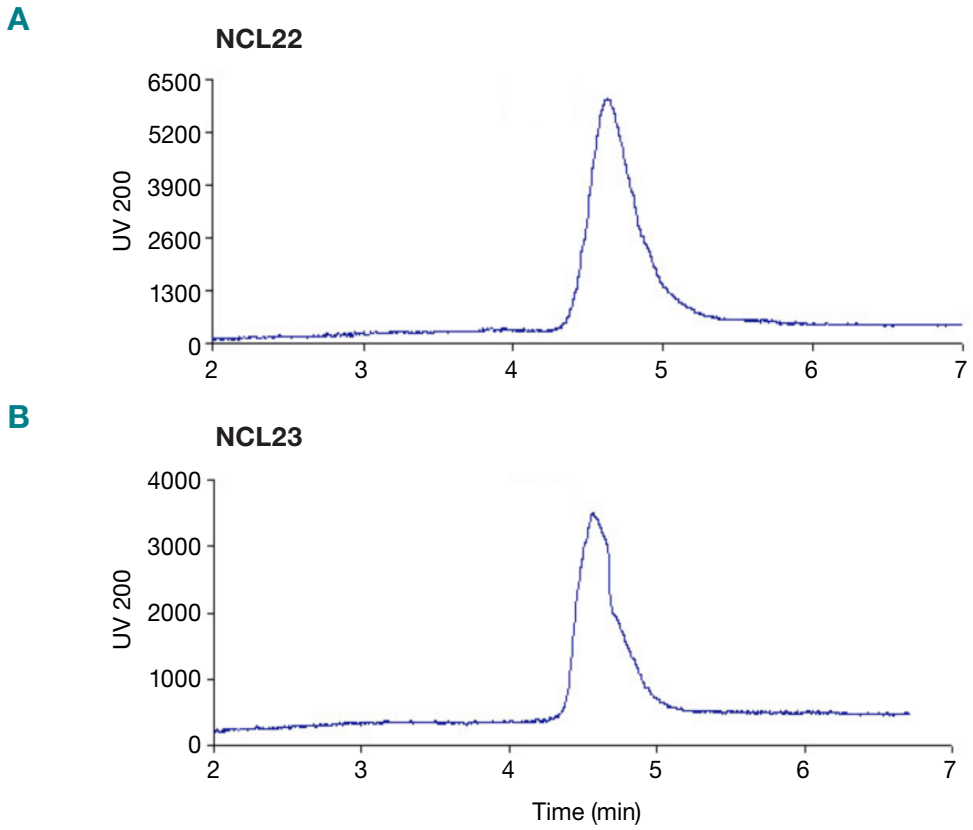

Figure 22. Typical electropherogram of (A) NCL22 and (B) NCL23. Sample concentration: 0.1 mg/mL in water; capillary: 40cm × 50 µm I.D; buffer: 20 mM sodium phosphate (pH = 7.4); separation voltage: -14kV; injection pressure: 0.5 psi/20s; detector: UV (wavelength 200 nm). CE is a powerful chromatographic technique that separates analytes on the basis of electrophoretic mobility differences. Mobility is determined by the mass-to-charge ratio of the analyte. CE has high separation efficiencies, high sensitivity, short run time and high automation capability. CE is extensively used to evaluate the molecular distribution of dendrimers, since the charge distribution and electrophoretic mobility often change upon dendrimer surface conjugation. Figure 22 shows that NCL22 and NCL23 have very similar electrophoretic mobilities (both are in the range of [4.3–5.2] × 10^{-4} cm^2 V^{-1} S^{-1}), which indicates they have the same charge/mass ratio.

Size Exclusion Chromatography (SEC) – Multiple Angle Laser Light Scattering (MALLS)

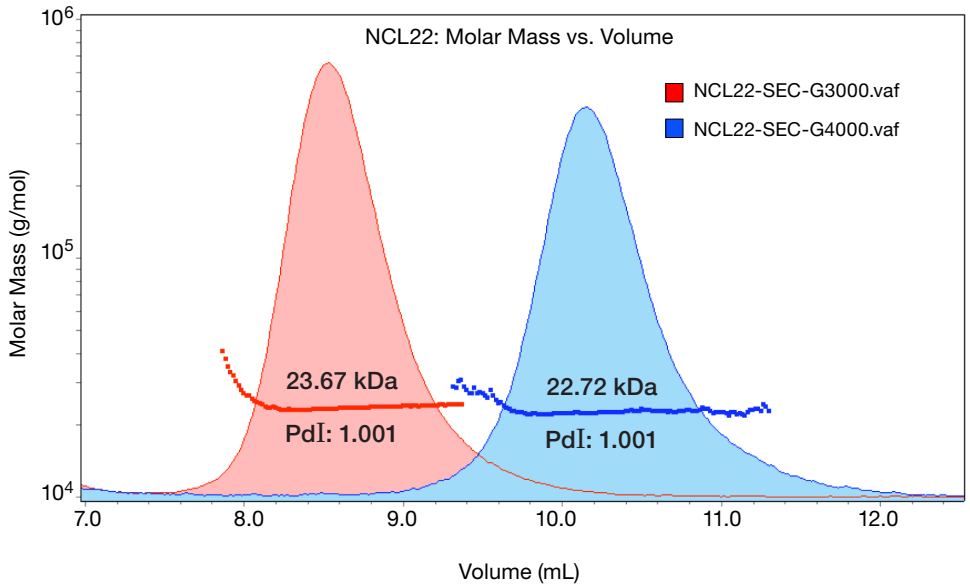

Figure 23. SEC chromatograms of NCL22 using two different columns. SEC is a separation technique used for determining the purity of a sample and is based on the molecular size of the sample components. Coupled with a MALLS and RI detectors, the molecular weight and root mean square (rms) radius can be determined for the fractionated sample.

Experimental conditions: The chromatographic system consisted of an isocratic pump (Agilent G1310A, Palo Alto, CA); Wyatt Injection System (Wyatt Technology, Santa Barbara, CA); and TosoHaas TSKgel Guard PWH 06762 (7.5 mm ID x 7.5 cm, 12 µm), TSKgel G3000PW 05762 (7.5 mm ID x 30 cm, 10 µm), and TSKgel G4000PW 05763 (7.5 mm ID x 30 cm, 17 µm) columns (TosoHaas, Montgomeryville, PA). The size exclusion column was connected in-line to a light scattering detector (DAWN EOS, 690 nm laser, Wyatt Technology, Santa Barbara, CA) and a refractive index detector (Optilab rEX, Wyatt Technology, Santa Barbara, CA). The isocratic mobile phase was PBS (1x, pH 7.5, Sigma D1408, St. Louis, MO) at a flow rate of 1 mL/min. Sample concentration was typically 2 mg/mL in PBS, and 100 µL was manually injected. Molecular weights were determined using Astra V 5.1.9.1 (Wyatt Technology, Santa Barbara, CA). A dn/dc value of 0.1677 mL/g (measured separately using the Wyatt Optilab rEX for NCL-22) was used for all molecular weight determinations.

The molar mass distribution plot for NCL-22 using two different size exclusion columns is shown. NCL-22 elutes faster using the G3000 column. The calculated molar mass for NCL-22 was 23.67 kDa and 22.72 kDa, and the polydispersity index was 1.001 and 1.001 using the G3000 and G4000 columns, respectively. The molecular weight determined by SEC-MALLS is slightly smaller than the theoretical molecular weight of 26.28 kDa.

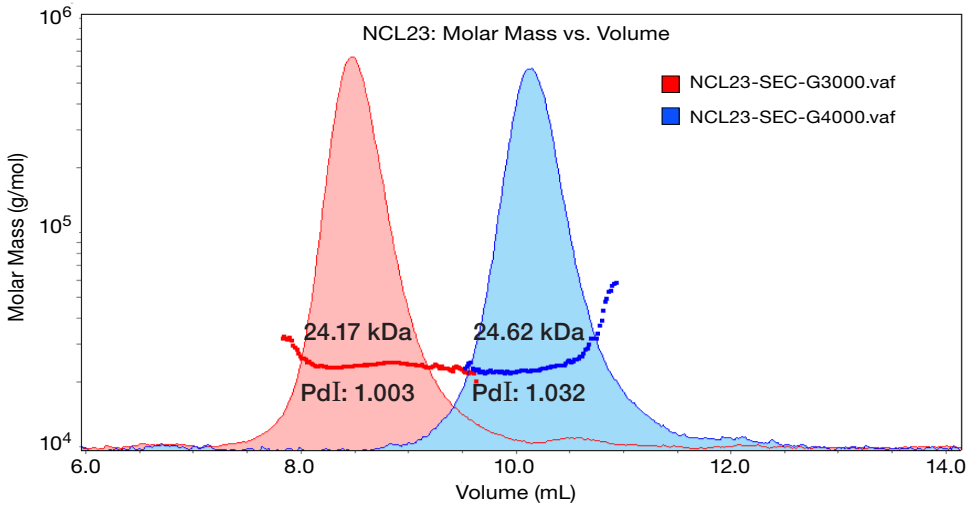

Figure 24. SEC chromatograms of NCL23 using two different columns. The molar mass distribution plot for NCL23 using 2 different size exclusion columns is shown. NCL23 elutes faster using the G3000 column. The calculated molar mass for NCL23 was 24.17 kDa and 24.62 kDa, and the polydispersity index was 1.003 and 1.032 using the G3000 and G4000 columns, respectively. The molecular weight determined by SEC-MALLS for NCL23 is very similar to that of NCL22. Since NCL23 is NCL22 with associated Magnevist, the results suggest that the Magnevist is no longer associated with the dendrimer after fractionation.

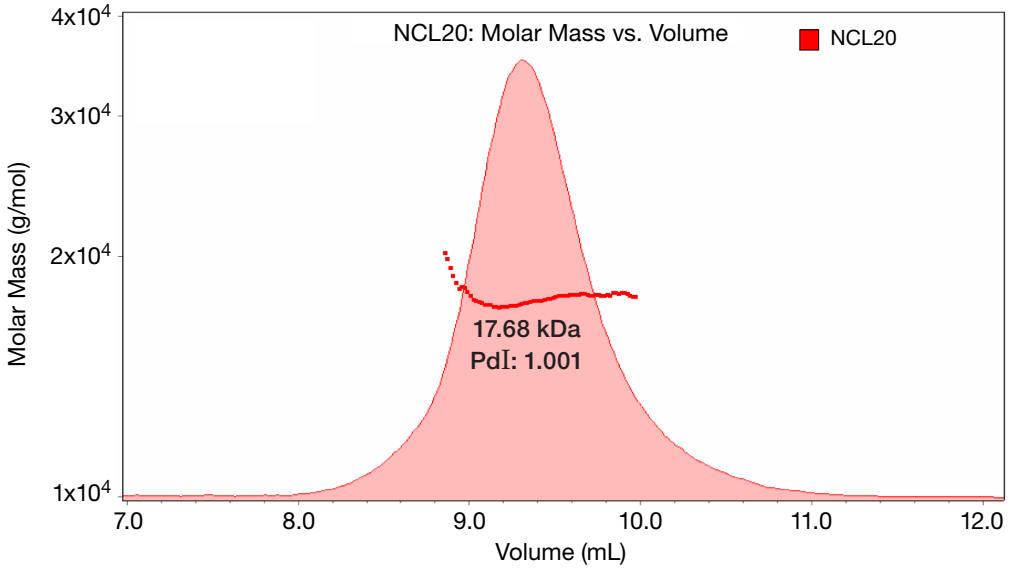

Figure 25. SEC chromatogram of NCL20. The molar mass distribution plot for NCL20 is shown. The calculated molar mass for NCL20 was 17.68 kDa, and the polydispersity index was 1.001. The molecular weight determined by SEC-MALLS is very close to the theoretical molecular weight of 18.15 kDa.

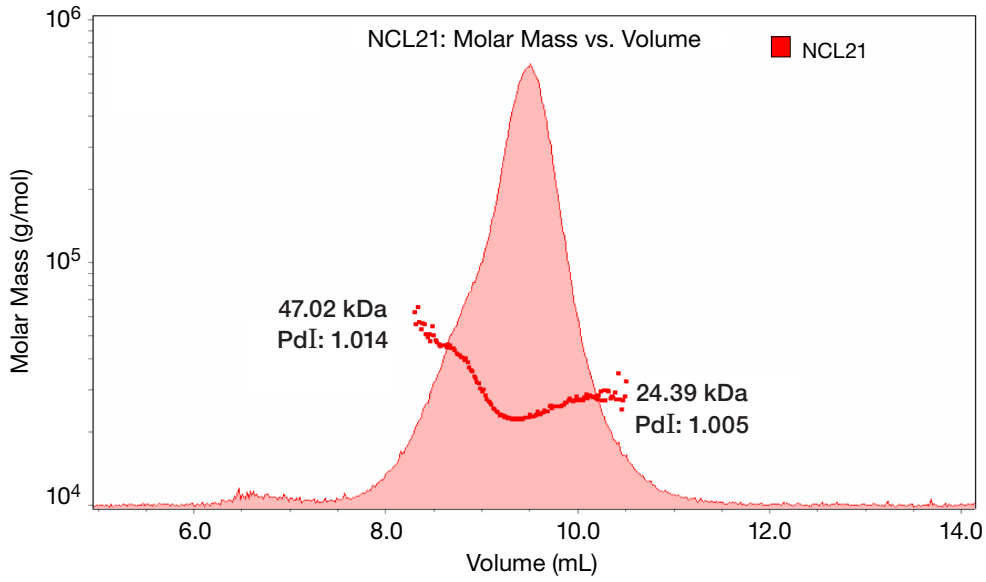

Figure 26. SEC chromatogram of NCL21. The molar mass distribution plot for NCL21 illustrates a main peak with a front shoulder (roughly between 7.5 and 9 mL). The calculated molar mass for the main peak and its front shoulder was 24.39 kDa and 47.02 kDa, respectively, and the polydispersity index was 1.005 and 1.014, respectively. The front shoulder has a molecular weight roughly double that of the main peak, suggesting that the front shoulder is a dimer. The molecular weight determined by SEC-MALLS for the monomer is slightly higher than the theoretical molecular weight of 22.31 kDa.

Asymmetrical Flow Field Flow Fractionation (AFFF) – Multi Angle Light Scattering (MALS)

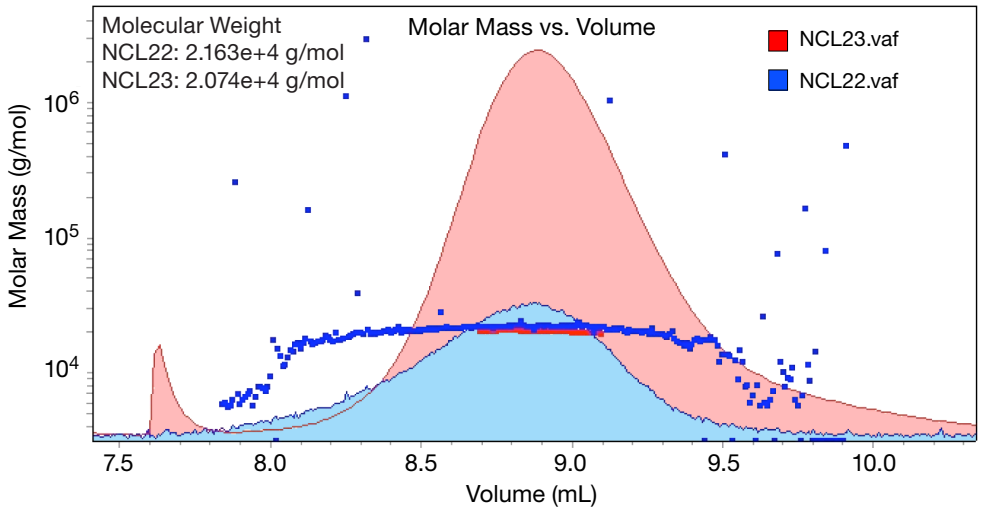

Figure 27. Molar mass versus elution time plot of NCL22 and NCL23 by AFFF-MALLS. Concentration of NCL22: 1 mg/mL in H_2O; concentration of NCL23: 2 mg/mL in PBS; Conditions: Injection volume: 100 µL; 10kDa regenerated cellulose membrane; 350 µm channel thickness; 1 mL/min channel flow; 3 mL/min cross-flow. AFFF is an innovative separation method for an efficient separation and characterization of nanoparticles, polymers and proteins that is both fast and gentle. When coupled with a MALLS system, the molar mass and rms radius can be obtained for the fractionated sample. The molar mass distribution plot shows that NCL22 and NCL23 have similar molar mass by using AFFF as a separation method. The calculated molar mass of NCL22 and NCL23 was 21.63 kDa and 20.74 kDa, and the polydispersity index was 1.046 and 1.078, respectively (the molar mass of both NCL22 and NCL23 was determined by using the dn/dc value of NCL22, which was measured using an RI detector).

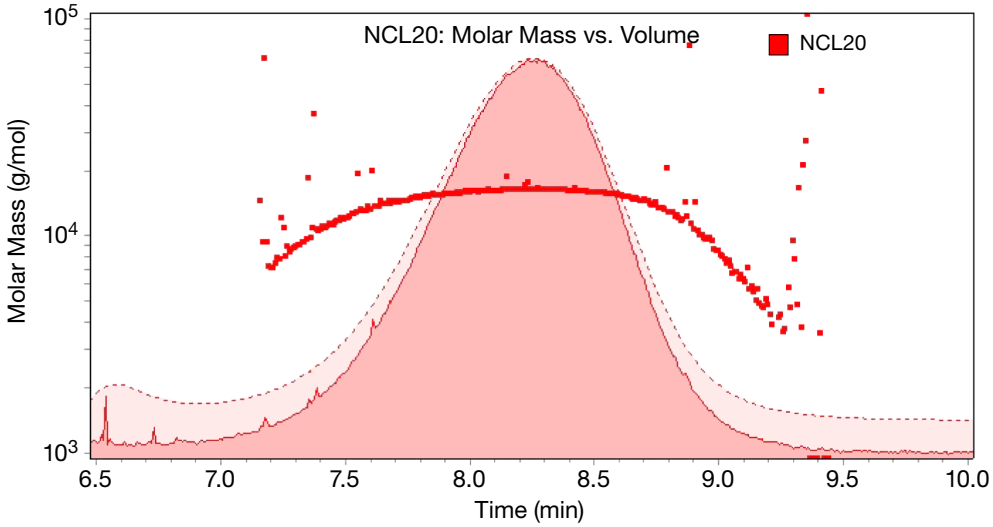

Figure 28. Molar mass versus elution time plot of NCL20 by AFFF-MALLS. Concentration: 3.38 mg/mL; Conditions: injection volume: 100 µL; 10kDa AFFF regenerated cellulose membrane, 350 µm channel thickness, 1 mL/min channel flow, 3mL/min cross-flow. The calculated molar mass for NCL20 was 15.1 kDa, and the polydispersity index was 1.077.

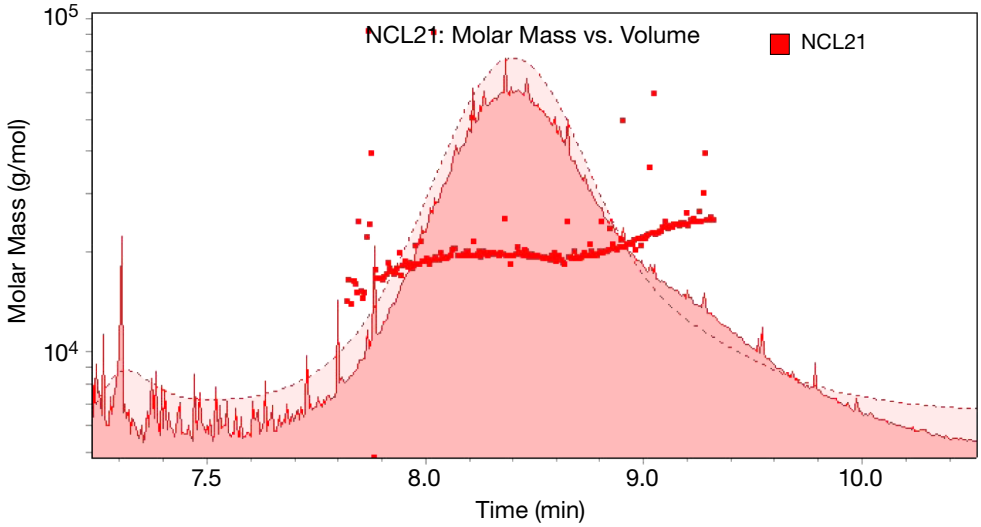

Figure 29. Molar mass versus elution time plot of NCL21 by AFFF-MALLS. Concentration: 2.7 mg/mL; Conditions: injection volume: 100 µL, 10kDa AFFF regenerated cellulose membrane, 350 µm channel thickness, 1 mL/min channel flow, 3 mL/min cross-flow. For molecular weight determinations, the dn/dc value is needed and was assumed to be the same as NCL22 (0.1677 mL/g). The calculated molar mass for the major peak and its shoulder peak was 23.9 kDa and 45.3 kDa, respectively, and the polydispersity index was 1.141 and 1.281, respectively. The shoulder peak has a molecular weight roughly double that of the major peak, which is indicative of a dimer.

MRI Relaxivity Measurements for NCL23 *(in vitro)*

A

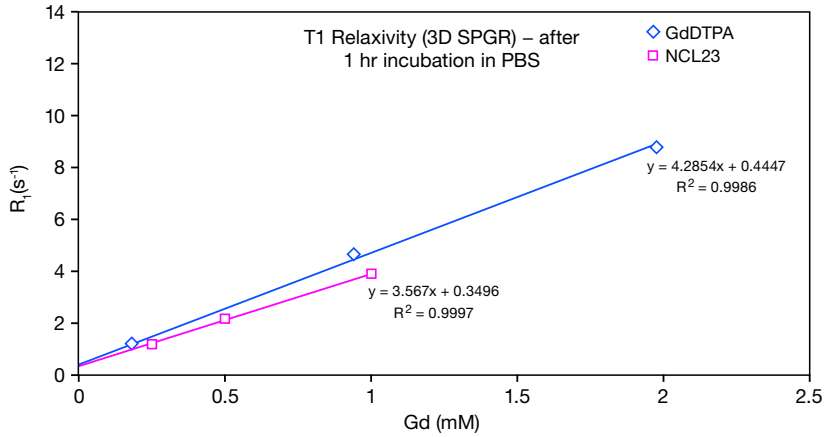

B

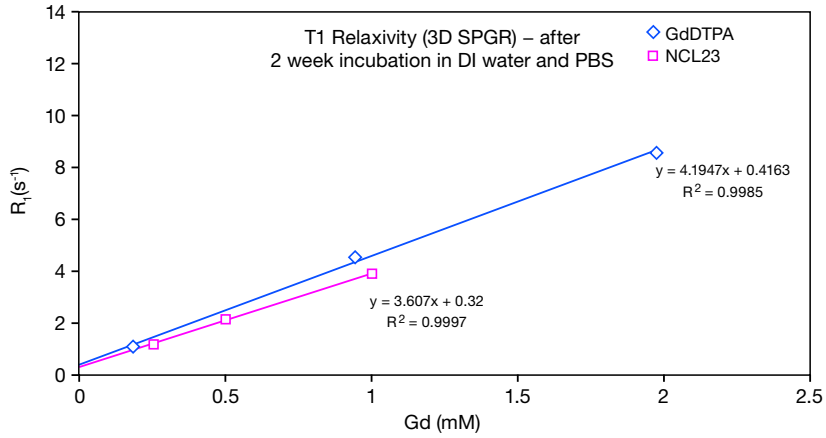

C

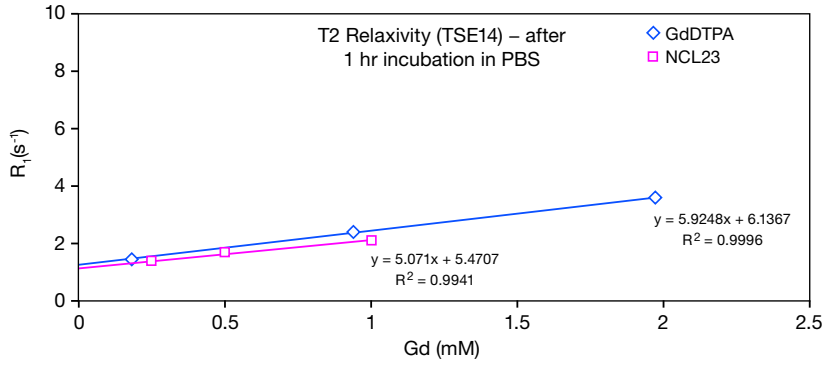

Figure 30. T1 and T2 relaxivity curves for NCL23. A 3 Tesla MRI was used for this study. The T1 (3D SPGR) and T2 (Spin echo) relaxivity measurements were taken on serial dilutions of NCL23 based on Gd content (0; 0.25; 0.5; 0.75; and 1 mM Gd). The stability of NCL23 in PBS was measured at 15, 30, 45 and 60 min, and two weeks after adding the aqueous DI water solution to PBS. The T1 and T2 relaxivity of the dendrimer-Magnevist complex (NCL23) is very close to that of Magnevist alone (Gd-DTPA). No change in T1 (Figure 30, A and B) and T2 (Figure 30, C) relaxivity was observed after one hour of incubation with PBS and two weeks of incubation in DI water and PBS. There is no evidence of change in relaxivity due to vendor formulation.

CYTOTOXICITY CHARACTERIZATION

SECTION SUMMARY

Nanoparticle biocompatibility was evaluated in the porcine renal proximal tubule cell line, LLC-PK1, and the human hepatocarcinoma cell line, Hep-G2. Cytotoxicity was determined as described in the NCL methods, LLC-PK1 Kidney Cytotoxicity Assay, and Hep-G2 Hepatocarcinoma Cytotoxicity Assay (GTA-1 and GTA-2, respectively). Briefly, test materials were diluted to the desired assay concentrations in cell culture media. Cells were preincubated for 24 h prior to adding test material, reaching an approximate confluence of 80%. Cells were exposed to test material for 6, 24 and 48 h, and cytotoxicity was determined using the MTT cell viability and LDH membrane integrity assays.

The maximum concentration of NCL22, NCL23 and NCL24 tested in the LLC-PK1 cytotoxicity study was 1 mg/mL. None of the materials tested produced a loss of cell viability greater than 50%, as measured by MTT cytotoxicity assay (Fig. 1). Treatment of cells with NCL22, NCL23 and NCL24 also resulted in a minimal loss of membrane integrity, as measured by LDH leakage (Fig.2), at the concentrations tested.

The maximum concentration of NCL22, NCL23 and NCL24 tested in the Hep-G2 cytotoxicity study was 5 mg/mL. At this maximum concentration, none of the materials tested produced a loss of cell viability greater than 50%, as measured by MTT cytotoxicity assay (Fig. 3). Treatment of cells with NCL22, 23 and 24 also resulted in a minimal loss of membrane integrity, as measured by LDH leakage (Fig.4), at the concentrations tested.

In summary, NCL22, NCL23 and NCL24 were found to be minimally cytotoxic, under the testing conditions utilized. Therefore, further *in vitro* mechanistic toxicology studies were not conducted.

MTT Cytotoxicity Assay in LLC-PK1 Cells (GTA-1)

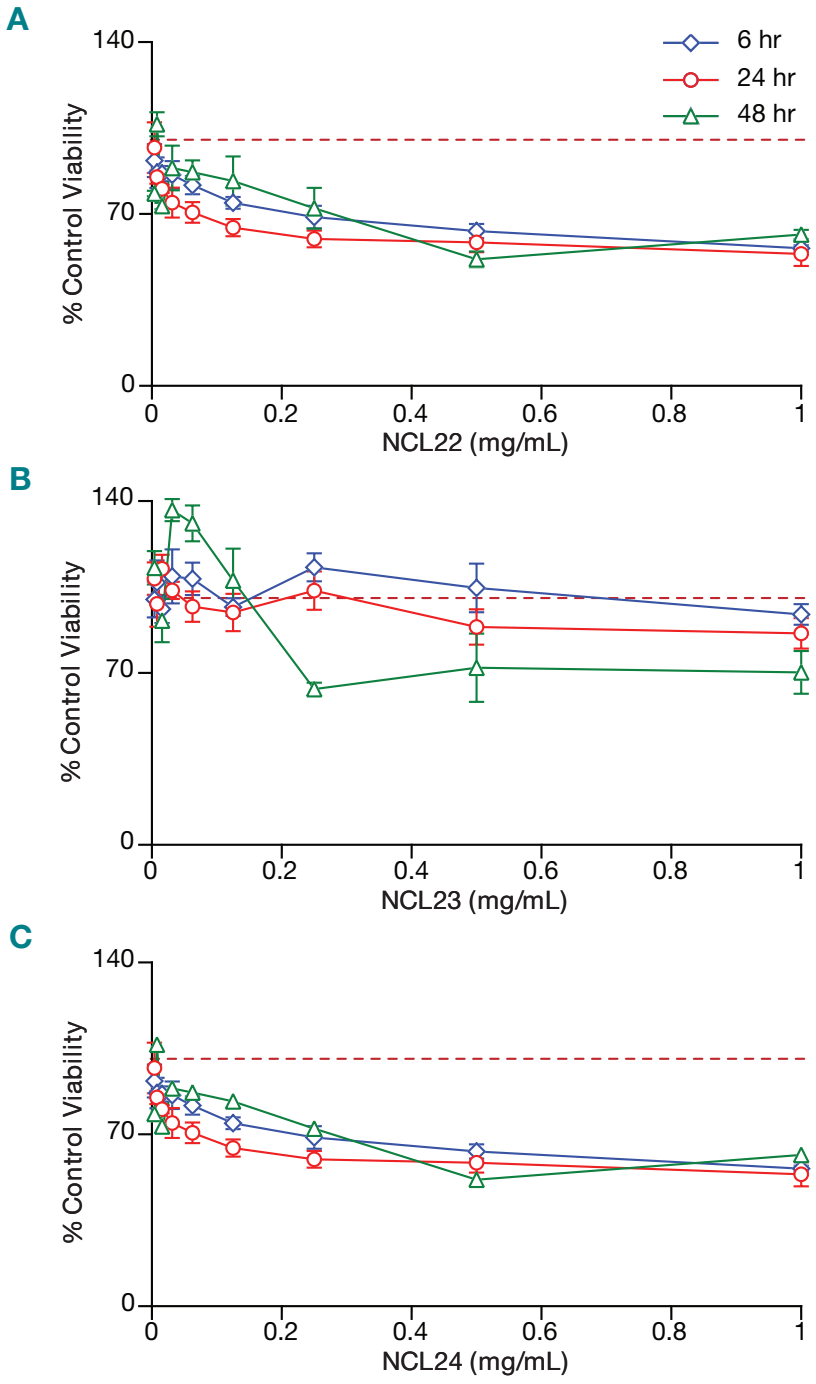

Figure 31. MTT cytotoxicity assay in LLC-PK1 cells. Porcine renal proximal tubule cells were treated for 6, 24, and 48 h with 0.004–1.0 mg/mL of test sample. Cytotoxicity was determined at each time point as described in the LLC-PK1 Kidney Cytotoxicity Assay (GTA-1). Dashed red line indicates 100% control viability.

LDH Cytotoxicity Assay in LLC-PK1 Cells (GTA-1)

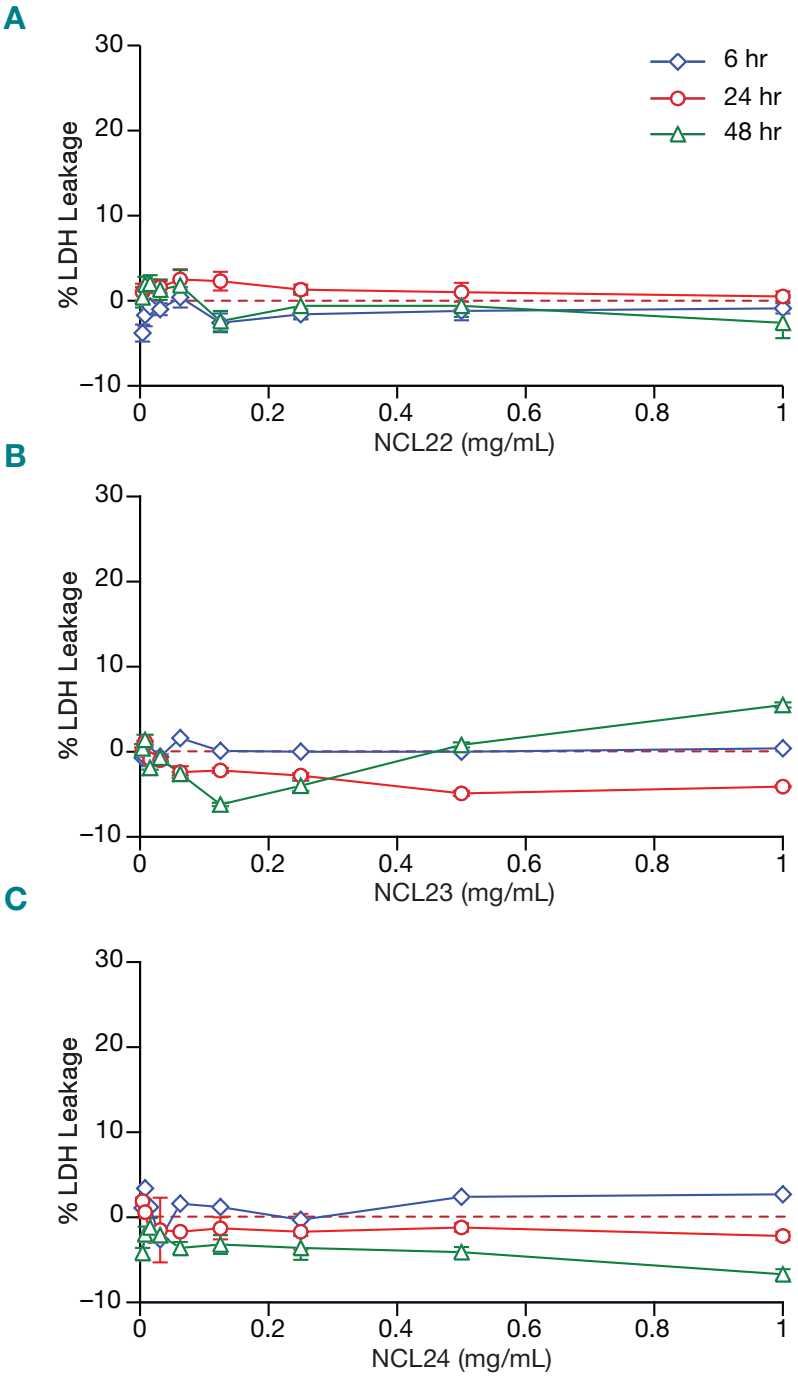

Figure 32. LDH cytotoxicity assay in LLC-PK1 cells. Porcine renal proximal tubule cells were treated for 6, 24, and 48 h with 0.004–1.0 mg/mL of test sample. Cytotoxicity was determined at each time point as described in the LLC-PK1 Kidney Cytotoxicity Assay (GTA-1). Dashed red line indicates 0% LDH leakage.

MTT Cytotoxicity Assay in Hep-G2 Cells (GTA-2)

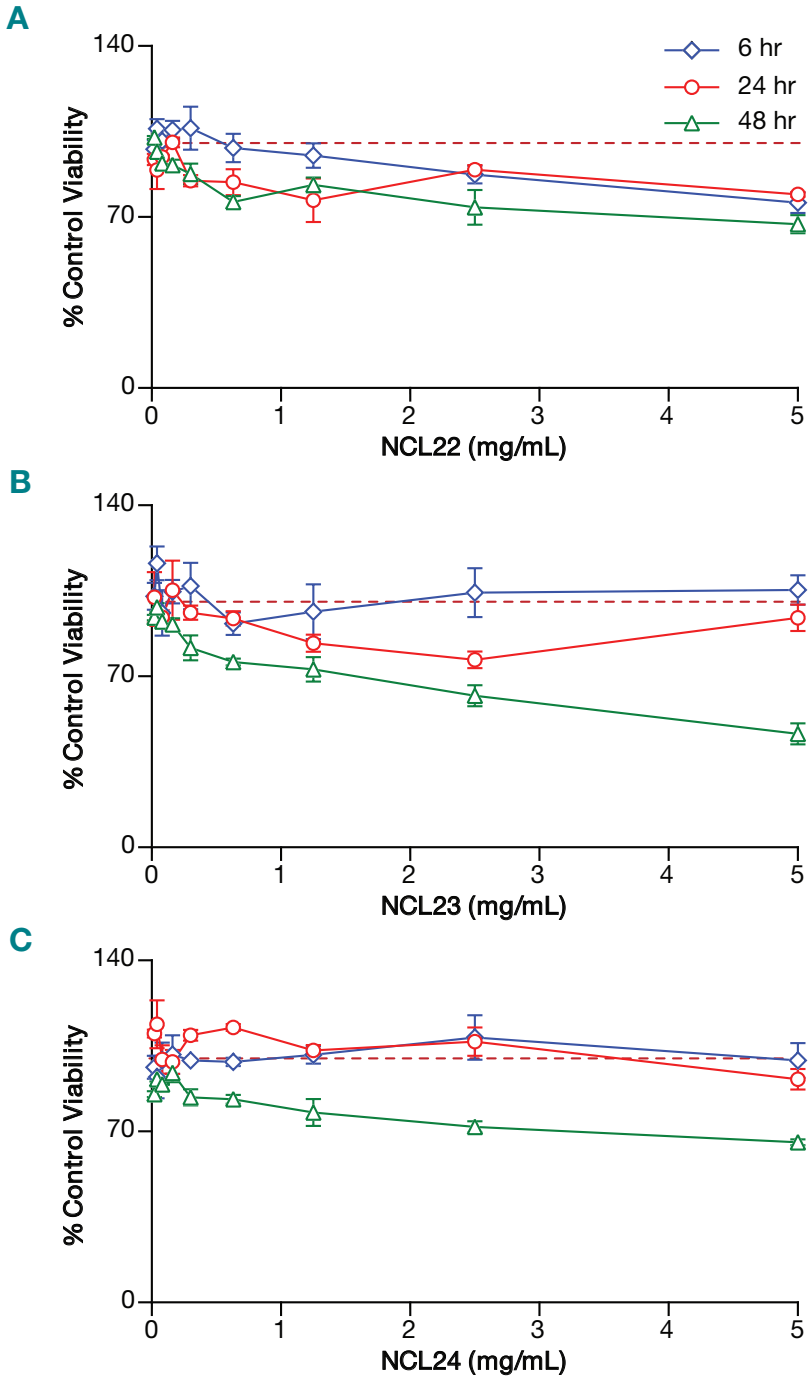

Figure 33. MTT cytotoxicity assay in Hep-G2 cells. Hep-G2 cells were treated for 6, 24, and 48 h with 0.02–5.0 mg/mL of test sample. Cytotoxicity was determined at each time point as described in the HEP G2 Hepatocarcinoma Cytotoxicity Assay (GTA-2). Dashed red line indicates 100% control viability.

LDH Cytotoxicity Assay in Hep-G2 Cells (GTA-2)

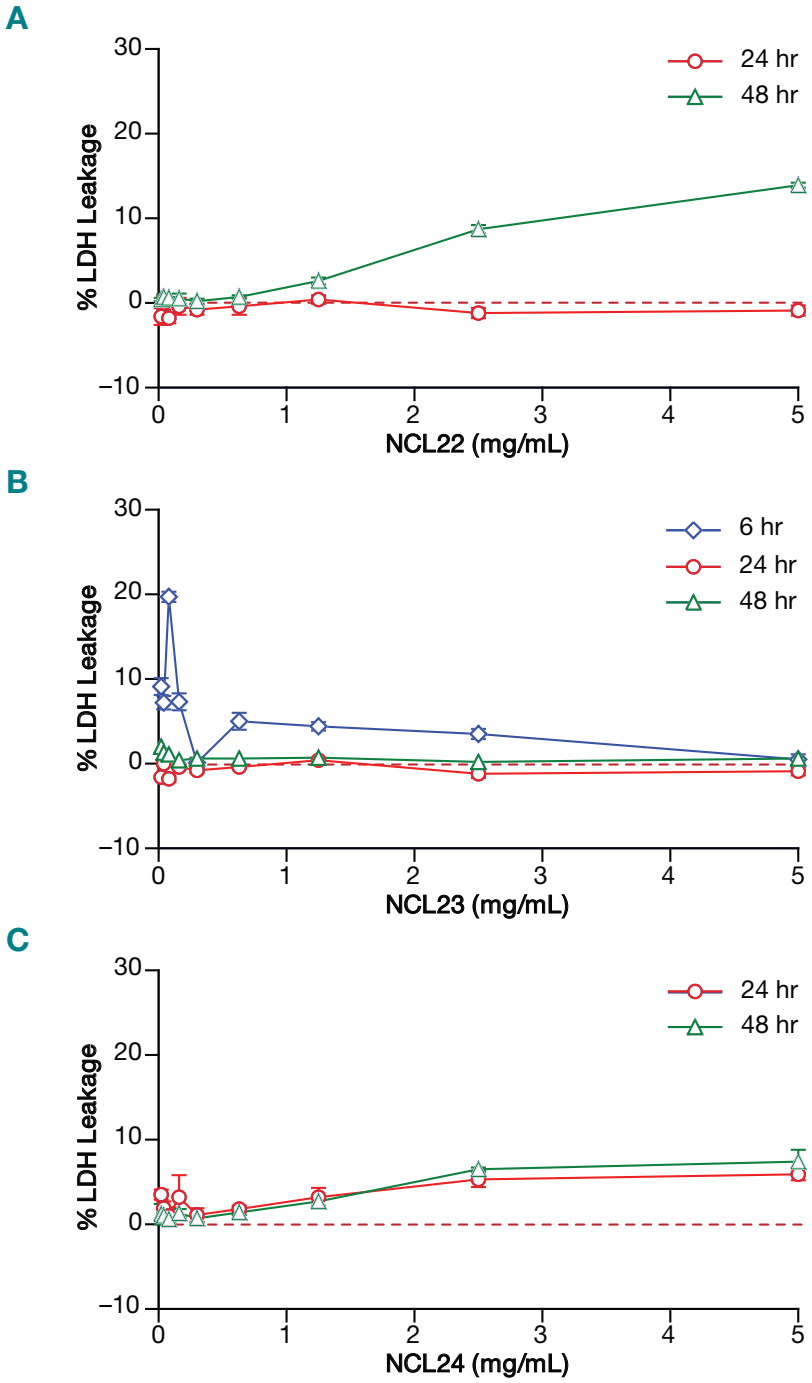

Figure 34. LDH cytotoxicity assay in Hep-G2 cells. Hep-G2 cells were treated for 6, 24, and 48 h with 0.02–5.0 mg/mL of test sample. Cytotoxicity was determined at each time point as described in the HEP G2 Hepatocarcinoma Cytotoxicity Assay (GTA-2). Dashed red line indicates 0% LDH leakage.

SECTION SUMMARY

Evaluation of biocompatibility at the level of the particle–blood interface and potential toxicity of NCL22, NCL23 and NCL24 to immune cells was performed using twelve *in vitro* immunotoxicity assays (Fig. 1). Test concentrations of NCL22, NCL23 and NCL24 for the immunotoxicity assays were selected based on dose-response curves obtained for these formulations in the GTA-1 general toxicity assay (Cytotoxicity Characterization, Fig. 1).

NCL Non-GLP *In Vitro* Immunotoxicity Tests

Interaction with plasma proteins (2D EF)	Macrophage/neutrophil function
Hemolysis	Phagocytosis
Effects on Complement	Inflammatory mediators
Effect on platelets	Chemotaxis
Coagulation	Oxidative burst
GM-CFU assay	Cytotoxic activity of NK cells
Leukocyte proliferation	

Figure 35. Summary of *in vitro* immunotoxicity assays. Results of these assays performed for NCL22, NCL23 and NCL24 are presented below.

Sterility

Sterility of nanoparticles was evaluated before initiating *in vitro* tests. Endotoxin levels in NCL22 and NCL23, determined by the Limulus Amebocyte Lysate (LAL) test, were found to be 0.093 and 0.236 EU/mg, respectively. Particles did not interfere with the LAL assay (Fig. 2).

No bacterial, yeast or mold contamination was found in the tested nanomaterials (Fig. 3).

Evaluation of potential contamination with mycoplasma was not possible due to particle interference with the assay detection system (Fig. 4).

Blood Contact Properties

NCL22, NCL23 and NCL24 did not disturb the integrity of red blood cells (Fig. 5) or cause platelet aggregation (Fig. 6A). NCL22 did not interfere with collagen-induced platelet aggregation, while high concentrations of NCL23 and NCL24 slightly increased aggregation of human platelets induced by collagen (Fig. 6B).

NCL22 and a low concentration of NCL23 did not cause myelosuppressive effects, while high concentrations of NCL23 and NCL24 resulted in a reduction in the CFU-GM colony number (Fig. 7).

Potential particle interference with plasma coagulation factors was evaluated using specimens obtained from three separate groups of healthy donors. In one of the three groups, high concentrations of NCL22, NCL23 and NCL24 delayed coagulation evaluated by APTT, Thrombin, and reptilase time assays (Fig. 8A). In the two other groups, test materials did not interfere with plasma coagulation (Figs. 8B and 8C).

The sample preparation protocol described in NCL method ITA-4 was modified in order to separate dendrimer-bound proteins from bulk plasma, because ultracentrifugation-based separation was not feasible for the dendrimer samples. The modified procedure consisted of dendrimer immobilization on ELISA plate. No protein was found to specifically bind to the dendrimer surface using this approach (Fig. 9). Other approaches were not evaluated due to the change in project status.

NCL22 and low concentrations of NCL23 did not induce complement activation, while high concentrations of NCL23 and NCL24 resulted in activation of complement (Fig. 10).

Effects on Immune Cell Function

NCL22, NCL23 and NCL24 did not induce leukocyte proliferation. When tested at concentrations of 1 mg/mL, NCL22 did not interfere with leukocyte proliferation induced by Phytohemaglutinin-M (PHA-M), while NCL23 inhibited the PHA-M–induced proliferation (Fig. 11). NCL24 at 1 mg/mL was toxic to cells.

NCL22, NCL23 and NCL24 did not induce oxidative burst in the murine macrophage cell model (Fig. 12). Test materials did not induce chemotaxis (Fig. 13).

NCL22, NCL23 and NCL24 were not internalized via phagocytic uptake in a model of the human HL-60 cell line model. NCL22 did not interfere with phagocytosis of zymosan A, while NCL23 and NCL24 suppressed phagocytic uptake of zymosan (Fig. 14).

None of the test materials was capable of inducing cytokines in human peripheral blood mononuclear cells after 24 or 48 h (Figures 15A and 15B). Dendrimer platform, NCL22, was also used for evaluation of potential immunosuppressive effects on Peripheral Blood Mononuclear Cells (PBMC). NCL22 failed to suppress LPS-induced cytokine production by PBMC (Fig. 15C).

NCL22 and low concentrations of NCL23 and NCL24 did not affect cytotoxicity of Natural Killer (NK) cells towards tumor K562 targets in a ^{51}Cr release assay. High concentrations of NCL23 and NCL24 slightly inhibited cytotoxicity of NK cells in the ^{51}Cr release assay (Fig. 16A).

The ability of the test materials to interfere with the cytotoxicity of NK cells was also assessed using a real-time cell electronic sensing technique (RT-CES). In this format, the adherent tumor cell line HepG2 was used as a target. Cells viability was monitored in real time for 48 h; the growth curves are presented in Figure 16B. The area under the curve (AUC) values were calculated for each sample and used to evaluate the percentage of cytotoxicity. No significant change in the cytotoxicity of NK cells towards tumor targets was observed by this approach for either NCL22, NCL23, or NCL24 (Fig. 16C).

Endotoxin Spike Recovery in the Presence of Dendrimer Particles (STE-1)

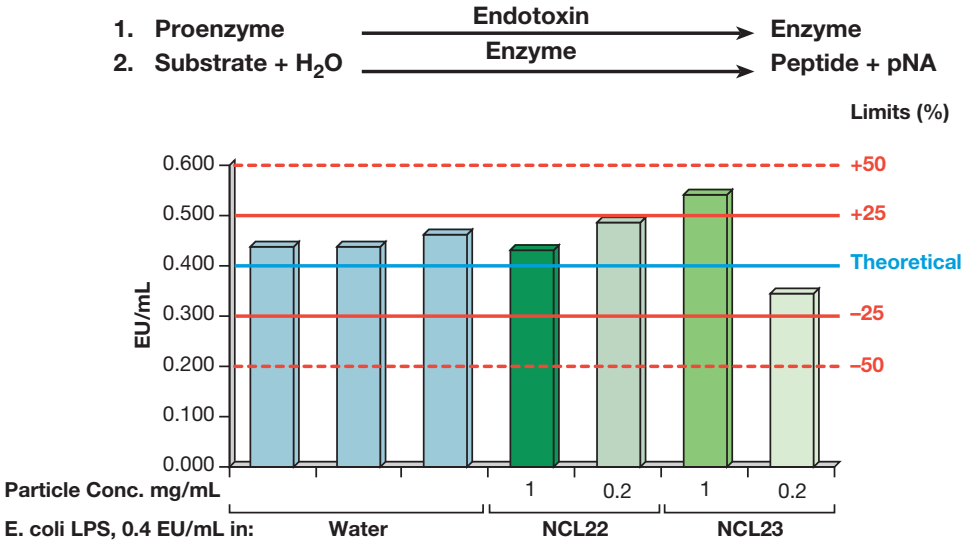

Figure 36. Endotoxin spike recovery in the presence of dendrimer particles (STE-1). Known concentration of endotoxin standard was spiked into water used for particle reconstitution, or into NCL22 or NCL23 solutions. Two concentrations of nanoparticles were used. Presented are results calculated from the standard curve of known endotoxin concentrations in water. The results are acceptable per FDA guidelines for LAL assay and demonstrate no nanoparticle interference with the assay detection system.

Microbial Sterility Test (STE-2)

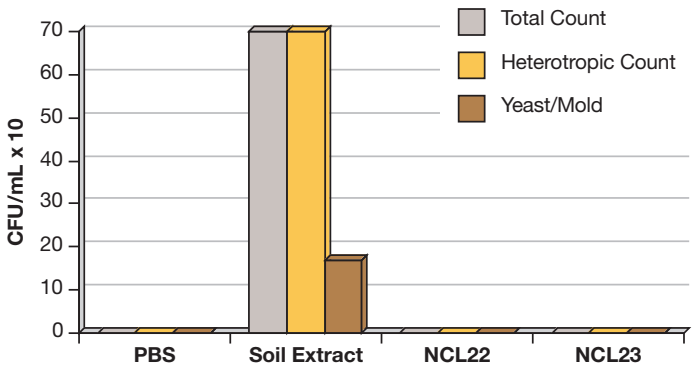

Figure 37. Microbial sterility test (STE-2). Preparations of NCL22 and NCL23 were found to be below limits of detection for bacterial, yeast, and mold contamination.

Mycoplasma Contamination Test (STE-3)

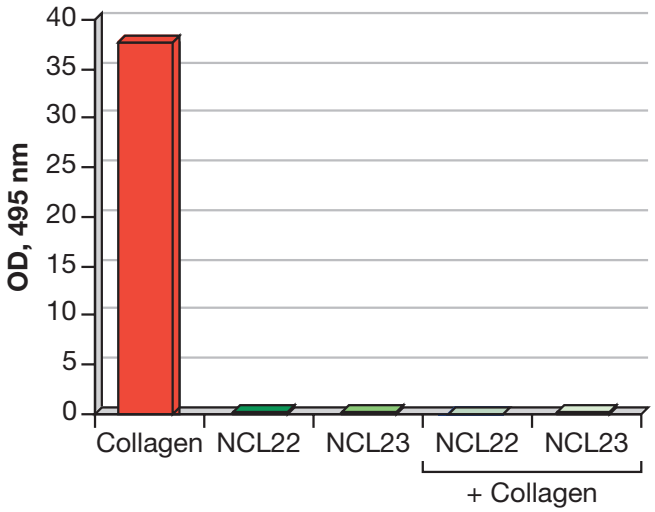

Figure 38. Mycoplasma contamination test (STE-3). The results of this assay revealed nanoparticle interference with the assay detection system. No mycoplasma contamination was detected in the presence of these particles.

Nanoparticle Hemolytic Properties (ITA-1)

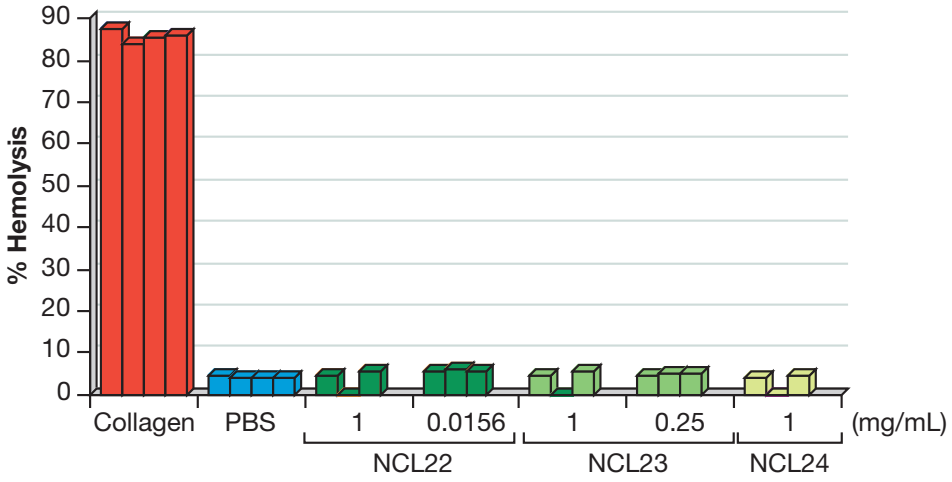

Figure 39. Analysis of nanoparticle hemolytic properties (ITA-1). NCL22 and NCL23 at either high (1 mg/mL) or low (0.0156 and 0.25 mg/mL, respectively) concentration, and NCL24 at 1 mg/mL were used to evaluate potential particle effects on the integrity of red blood cells. Three independent samples were prepared for each nanoparticle concentration and analyzed in duplicate (%CV < 20). Each bar represents the mean of duplicate results. Triton X-100 was used as a positive control. PBS was used to reconstitute nanoparticles and represented the negative control. Neither nanoparticle sample revealed hemolytic properties.

Nanoparticle Ability to Induce Platelet Aggregation (ITA-2)

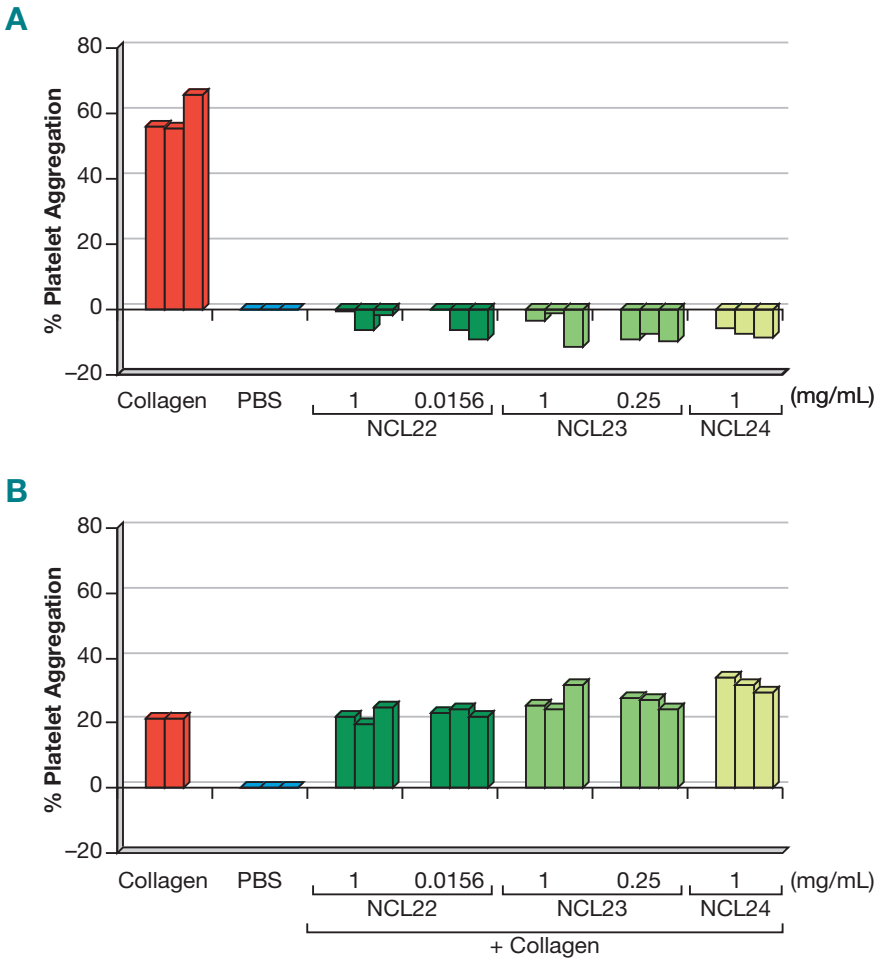

Figure 40. (A) Analysis of nanoparticle ability to induce platelet aggregation (ITA-2). NCL22 and NCL23 at either high (1 mg/mL) or low (0.0156 and 0.25 mg/mL, respectively) concentration, and NCL24 at 1 mg/mL were used to evaluate potential particle effects on the cellular component of the blood coagulation cascade. For each nanoparticle concentration, three independent samples were prepared and analyzed in duplicate (%CV < 20%). Each bar represents the mean of duplicate results. The results demonstrate that neither nanoparticle sample is capable of inducing platelet aggregation. Collagen and PBS were used as a positive and negative control, respectively. **(B) Analysis of nanoparticle effect on collagen-induced platelet aggregation (ITA-2).** NCL22 and NCL23 at either high (1 mg/mL) or low (0.0156 and 0.25 mg/mL, respectively) concentration, and NCL24 at 1 mg/mL were used to evaluate potential particle interference with platelet aggregation caused by a known activator. For each nanoparticle concentration, three independent samples were prepared and analyzed in duplicate (%CV < 20%). Each bar represents the mean of duplicate results. The results demonstrate that high doses of NCL23 and NCL24 enhanced collagen-induced platelet aggregation, while low concentrations of these particles did not disturb the process. NCL22 at both high and low doses did not interfere with collagen-induced platelet aggregation.

Nanoparticle Toxicity to Bone Marrow Cells (ITA-3)

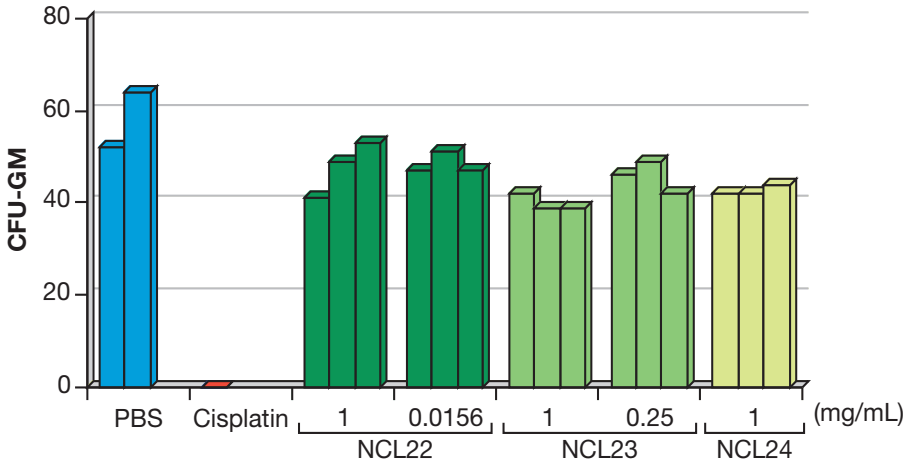

Figure 41. Analysis of nanoparticle toxicity to bone marrow cells (ITA-3). NCL22 and NCL23, at either high (1 mg/mL) or low (0.0156 and 0.25 mg/mL, respectively) concentration, and NCL24 at 1mg/mL were used to evaluate potential particle effects on the formation of granulocyte-macrophage colonies from bone marrow precursors. For each nanoparticle concentration, three independent samples were prepared and analyzed in duplicate (%CV < 20%). Each bar represents the mean of duplicate results. The results demonstrate that NCL22 and a low concentration of NCL23 are not myelosuppressive, while a high concentration of NCL23 and NCL24 suppresses CFU-GM formation ($p<0.05$). Cisplatin and PBS were used as a positive and negative control, respectively.

Nanoparticle Effect on Coagulation (ITA-12)

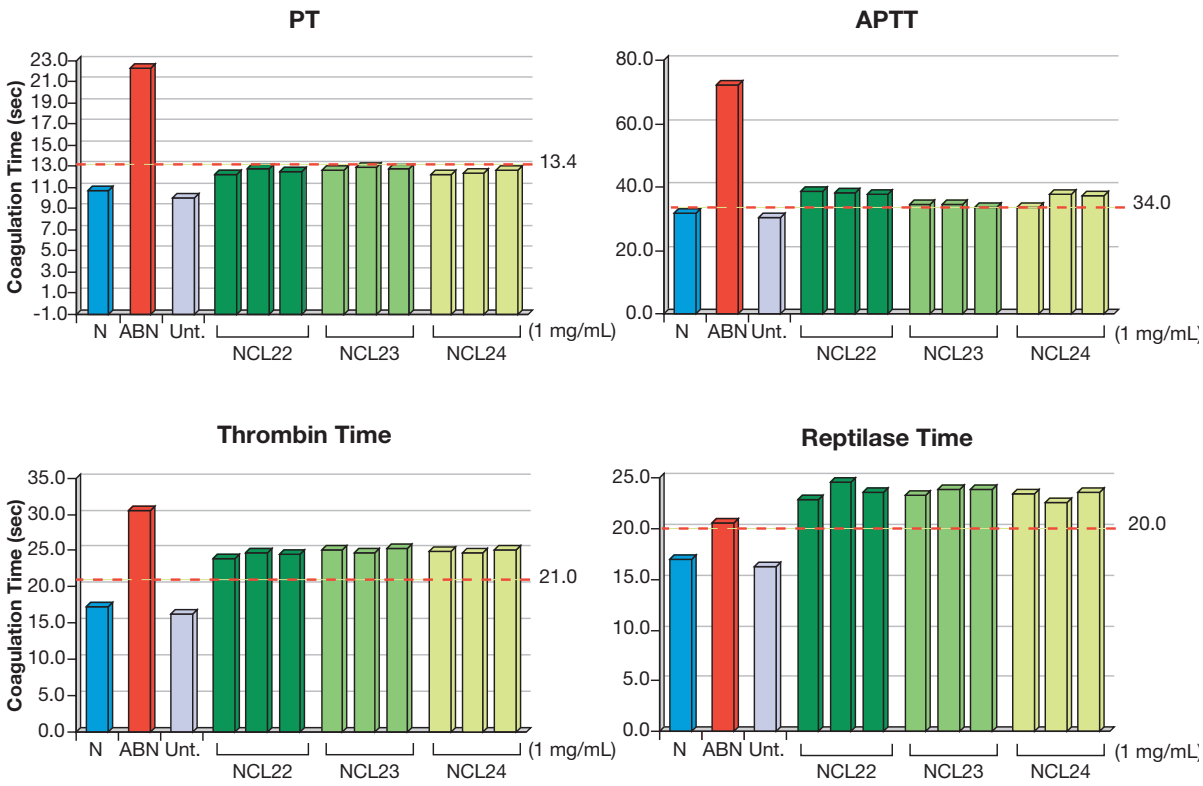

Figure 42A. Analysis of nanoparticle effect on coagulation - donor group 1 (ITA-12). NCL22, NCL23, and NCL24 at high (1mg/mL) concentrations were used to evaluate potential particle effects on the biochemical component of the blood coagulation cascade (prothrombin time [PT]; activated partial thromboplastin time [APTT]; Thrombin time and Reptilase time). For each nanoparticle, three independent samples were prepared and analyzed in duplicate (%CV < 5%). Each bar represents the mean of duplicate results. Normal plasma standard (N) and abnormal plasma standard (ABN) were used for the instrument control. Plasma pooled from at least three donors was either untreated (Unt.) or treated with nanoparticle preparations NCL22, NCL23, or NCL24. The dotted red line indicates the clinical standard cut-off for normal coagulation time for each of the tests. The results demonstrate that high concentrations of each nanoparticle sample delay coagulation time of plasma derived from donor group 1 above clinically acceptable standard in APTT, thrombin time and reptilase time tests.

Nanoparticle Effect on Coagulation (ITA-12)

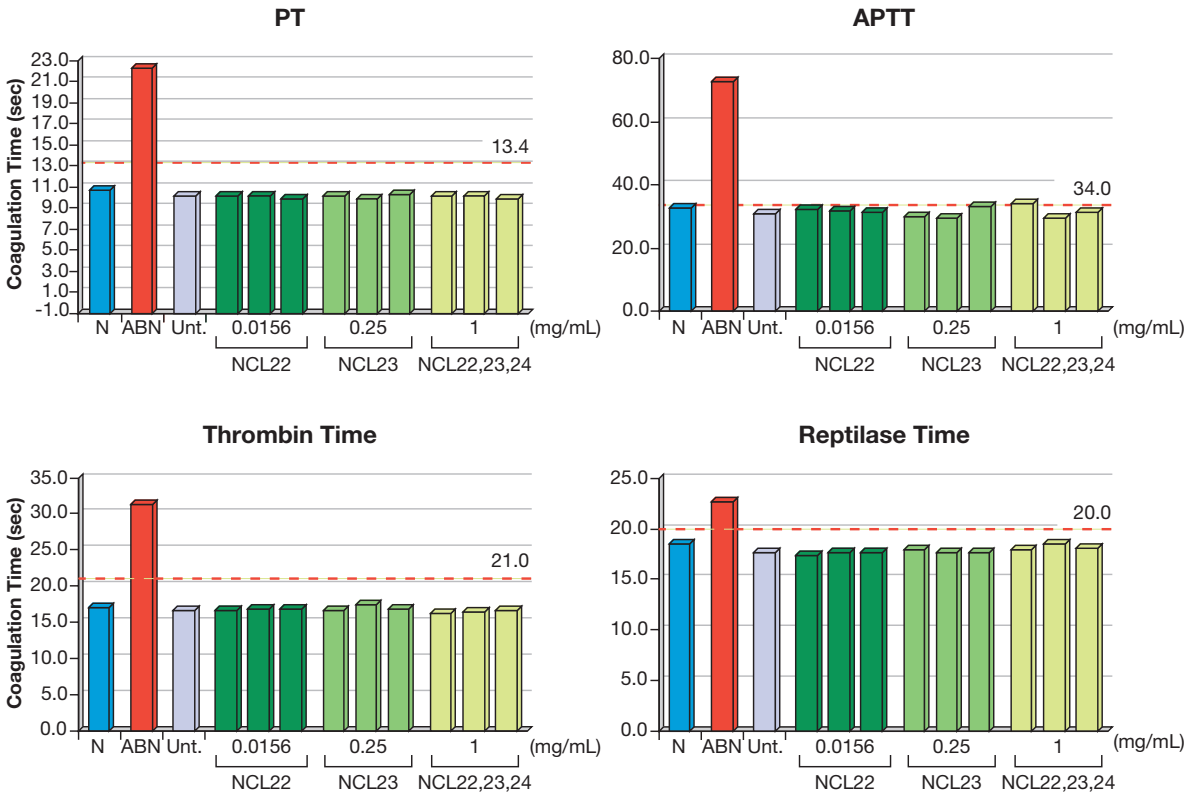

Figure 42B. Analysis of nanoparticle effect on coagulation - donor group 2 (ITA-12). NCL22 and NCL23 at low concentrations (0.0156 and 0.25 mg/mL, respectively) were used to evaluate potential particle effects on blood coagulation. For each nanoparticle concentration, three independent samples were prepared and analyzed in duplicate (%CV < 5%). Each bar represents the mean of duplicate results. The normal plasma standard (N) and abnormal plasma standard (ABN) were used for the instrument control. Plasma pooled from at least three donors was either untreated (Unt.) or treated with nanoparticle preparations NCL22 or NCL23. Plasma samples exposed to high concentrations of NCL22, NCL23, and NCL24 were also included in the analysis; one sample of each nanoparticle formulation at high concentration was prepared and analyzed in duplicate (%CV < 5%). Each bar represents the mean of duplicate results. The dotted red line indicates the clinical standard cut-off for normal coagulation time for each of the tests. The results demonstrate that, in this group of donors, neither nanoparticle test sample interferes with coagulation.

Nanoparticle Effect on Coagulation (ITA-12)

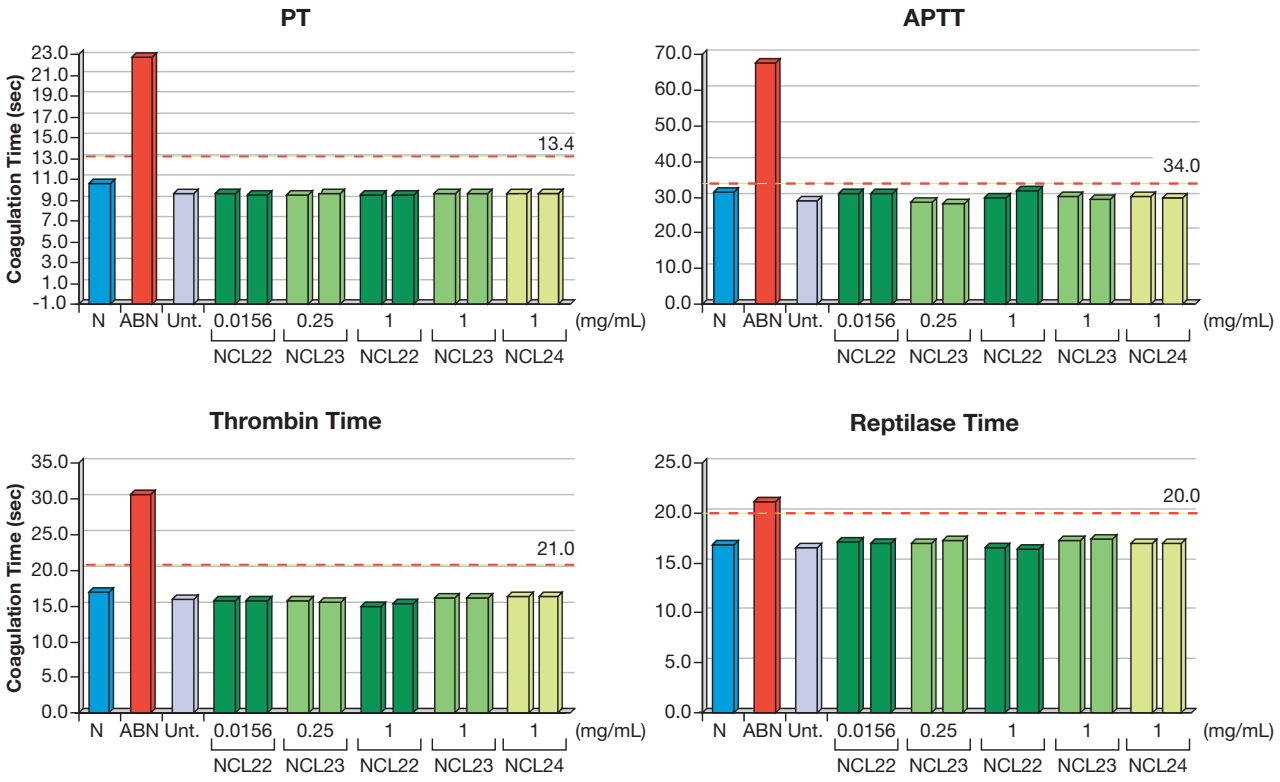

Figure 42C. Analysis of nanoparticle effect on coagulation - donor group 3 (ITA-12). NCL22 and NCL23 at low concentrations (0.0156 and 0.25 mg/mL, respectively) and NCL22, NCL23 and NCL24 at high concentration (1mg/mL) were used to evaluate potential particle effects on blood coagulation. For each nanoparticle concentration, two independent samples were prepared and analyzed in duplicate (%CV < 5%). Each bar represents the mean of duplicate results. The normal plasma standard (N) and abnormal plasma standard (ABN) were used for the instrument control. Plasma pooled from at least three donors was either untreated (Unt.) or treated with nanoparticle preparations NCL22, NCL23, and NCL24. The dotted red line indicates the clinical standard cut-off for normal coagulation time for each of the tests. The results demonstrate that, in this group of donors, neither nanoparticle test sample interfered with coagulation.

Interaction with Plasma Proteins (ITA-4)

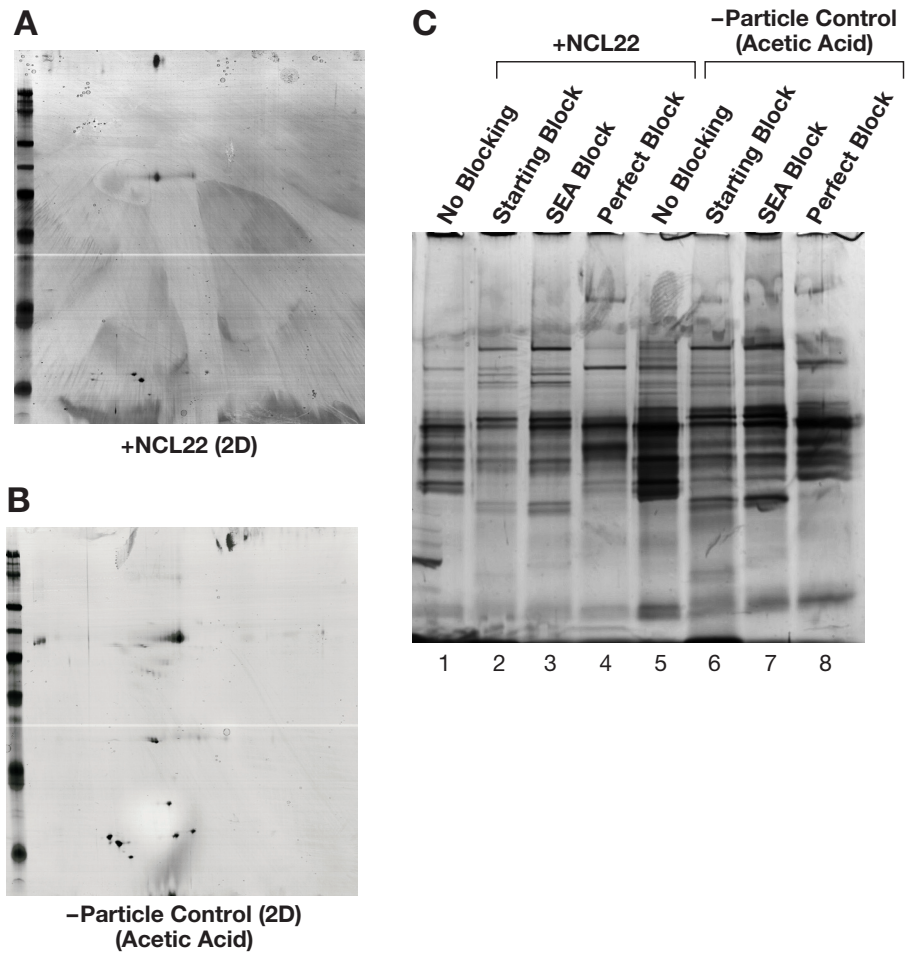

Figure 43. Interaction with plasma proteins (ITA-4). NCL22 was immobilized on a CovaLink ELISA plate in order to achieve separation of particle-bound proteins from bulk plasma. Proteins isolated from plates coated with NCL22 (A) or acetic acid (B) without any blocking buffers were then analyzed by 2D PAGE. Acetic acid was used as a negative control (C). During method development, several blocking buffers were tested to block unspecfic binding sites on the ELISA plate. The results suggest that NCL22 acts as a blocking agent. No proteins spots specific for NCL22 were identified using these conditions.

Complement Activation (ITA-5)

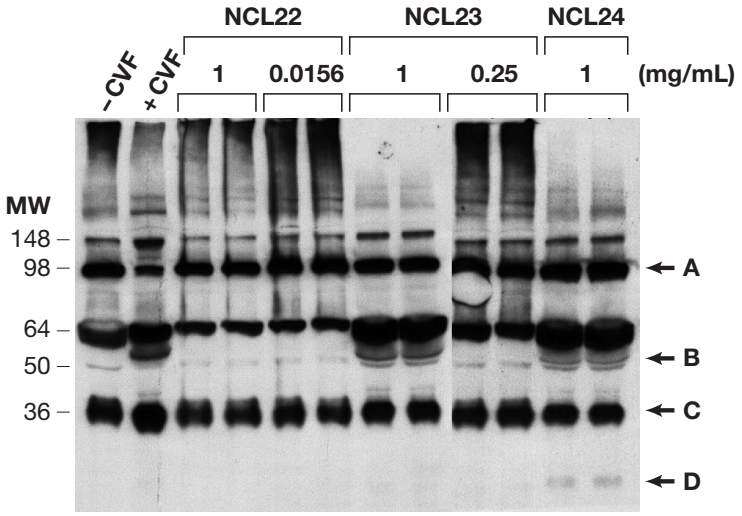

Figure 44. Analysis of complement activation (ITA-5). NCL22, NCL23 and NCL24 were tested for their ability to activate a complement. PBS and cobra venom factor (CVF) were used as the negative and positive control, respectively. NCL22 at both concentrations and NCL23 at low concentration did not induce complement activation, evidenced by an intensity of bands A and C that was similar to that of the negative control. NCL23 and NCL24 at 1mg/mL induced complement activation, evidenced by the appearance of split product (bands B and D) that was similar to that of the positive control.

Nanoparticle Effect on Leuckocyte Proliferation (ITA-6)

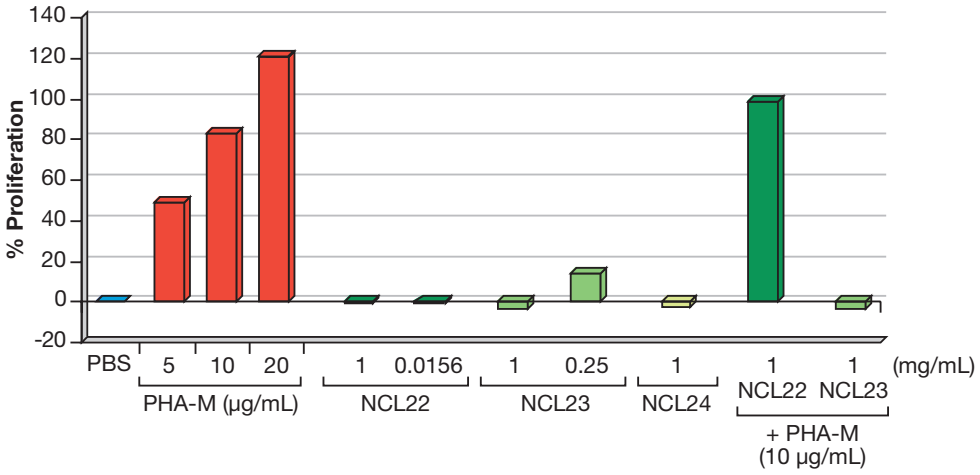

Figure 45. Analysis of nanoparticle effect on leuckocyte proliferation (ITA-6). NCL22, NCL23, and NCL24 did not induce leukocyte proliferation. Phytohemaglutinin-M (PHM) was used as a positive control for proliferation induction. For each nanoparticle concentration, three independent samples were prepared and analyzed in duplicate (%CV < 25%). Each bar represents the mean of duplicate results. NCL22 did not suppress proliferation induced by PHA-M, while NCL23 at 1mg/mL suppressed PHA-M–induced proliferation. PBS was used as a negative control.

Nitric Oxide Production by Macrophages (ITA-7)

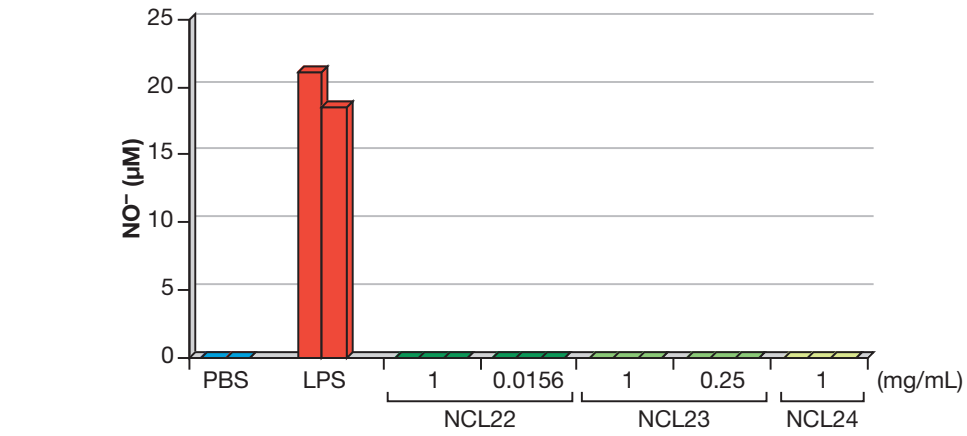

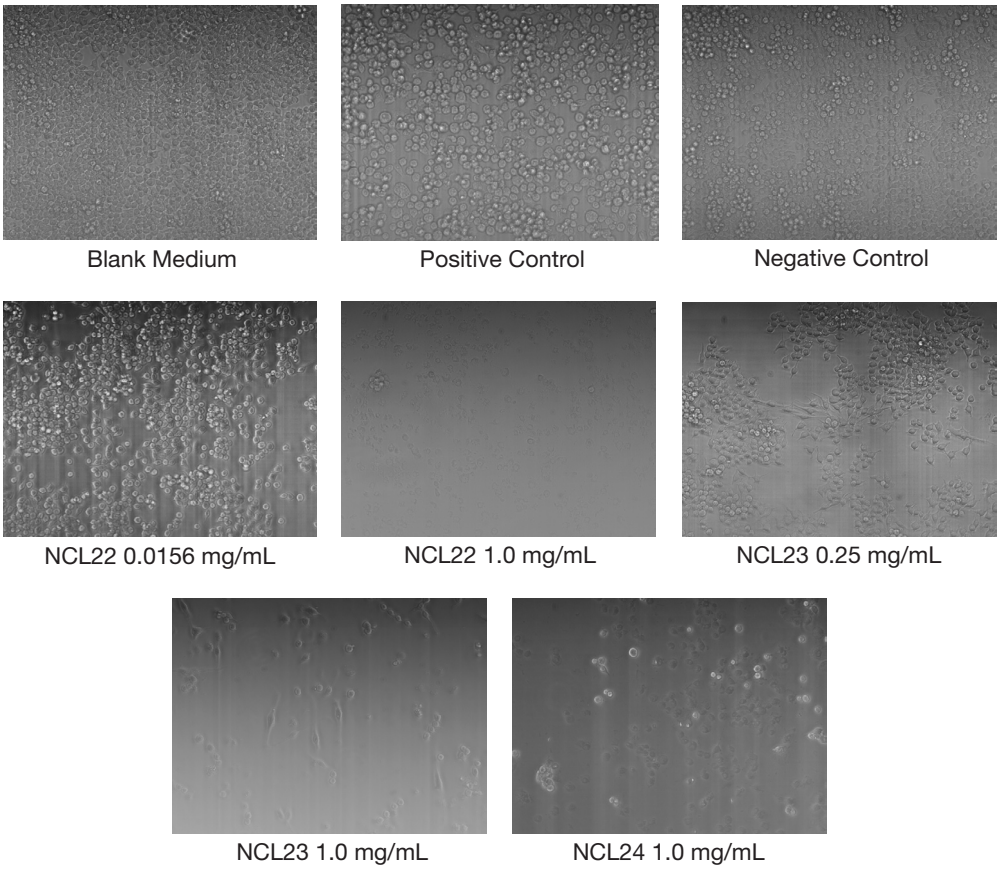

Figure 46. Analysis of nitric oxide (NO) production by macrophages (ITA-7). NCL22 and NCL23 were analyzed at high (1 mg/mL) and low (0.0156 and 0.25 mg/mL respectively) concentrations; NCL24 was analyzed at 1 mg/mL. For each concentration, three independent samples were prepared and analyzed in duplicate (%CV < 25%). Each bar represents the mean of duplicate results. NCL22, NCL23, and NCL24 did not induce NO production. At the high concentration NCL22, NCL23, and NCL24 were toxic for the RAW 264.7 macrophage cell line. PBS and bacterial LPS were used as a negative and positive control, respectively.

Nanoparticle Effect on Chemotaxis (ITA-8)

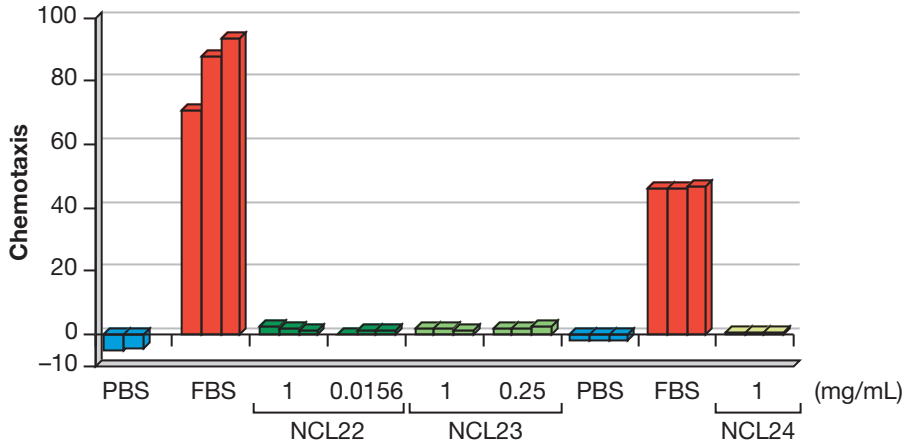

Figure 47. Analysis of nanoparticle effect on chemotaxis (ITA-8). NCL22, NCL23 and NCL24 did not induce chemotaxis of HL-60 macrophage-like cells. PBS and FBS were used as negative and positive controls, respectively.

Phagocytosis Assay (ITA-9)

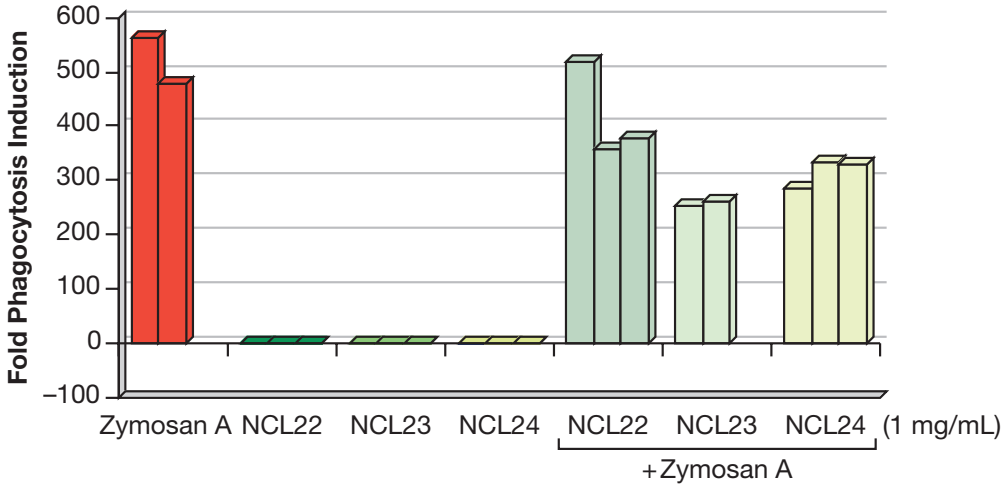

Figure 48. Phagocytosis assay (ITA-9). NCL22 and NCL23 were analyzed at high (1 mg/mL) and low (0.0156 and 0.25 mg/mL respectively) concentrations; NCL24 was analyzed at 1 mg/mL. For each concentration, three independent samples were prepared and analyzed in duplicate (%CV < 25%). Each bar represents the mean of duplicate results. Zymosan A was used as positive control. NCL22, NCL23, and NCL24 were not phagocytosed by macrophages. NCL22 did not affect phagocytic uptake of Zymosan A, while NCL23 and NCL24 suppressed phagocytosis of Zymosan A. All particles were tested at a concentration of 1 mg/mL.

Cytokine Secretion by PBMC (ITA-10)

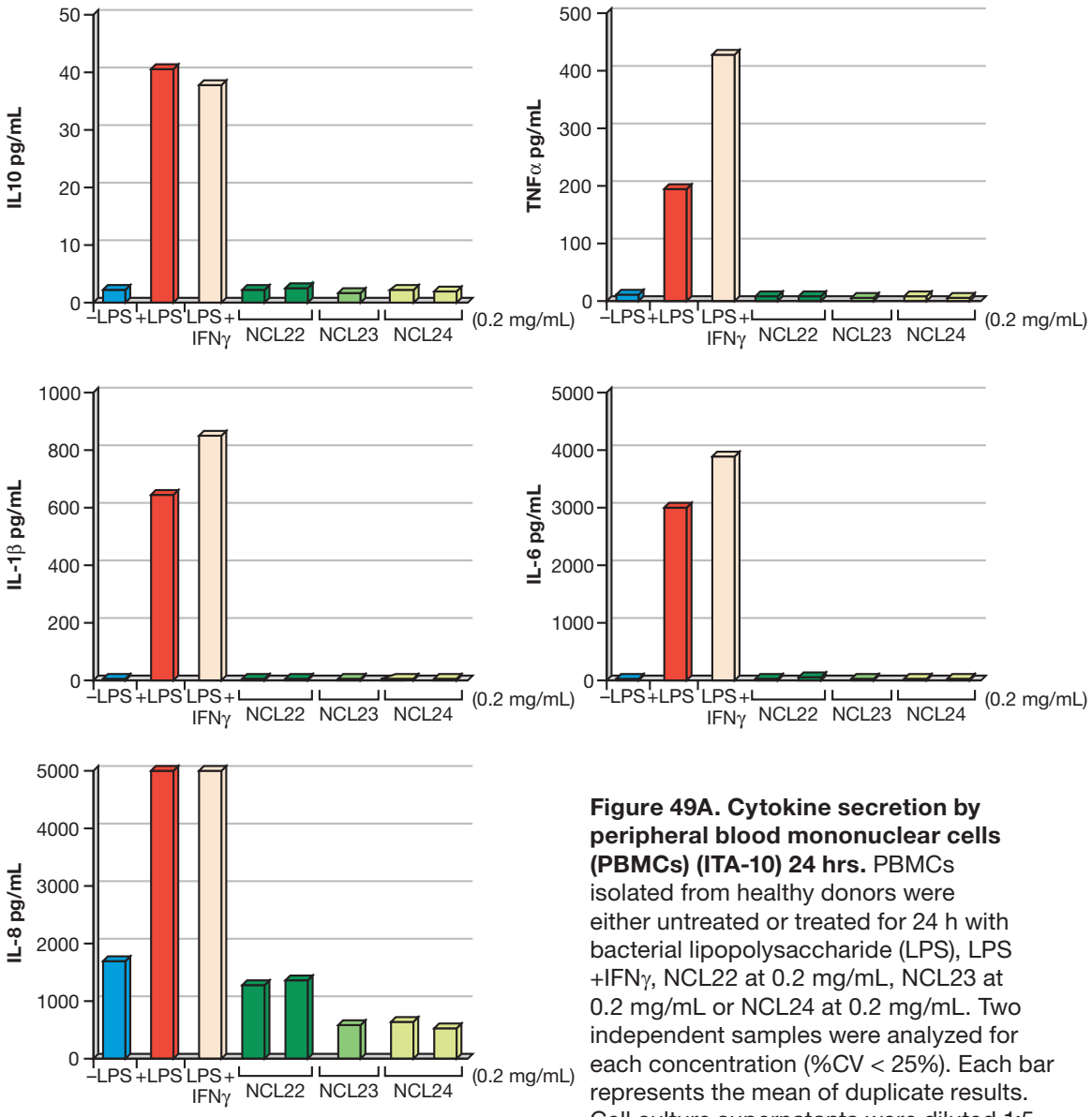

Figure 49A. Cytokine secretion by peripheral blood mononuclear cells (PBMCs) (ITA-10) 24 hrs. PBMCs isolated from healthy donors were either untreated or treated for 24 h with bacterial lipopolysaccharide (LPS), LPS +IFNγ, NCL22 at 0.2 mg/mL, NCL23 at 0.2 mg/mL or NCL24 at 0.2 mg/mL. Two independent samples were analyzed for each concentration (%CV < 25%). Each bar represents the mean of duplicate results. Cell culture supernatants were diluted 1:5 and analyzed by flow cytometry using a Cytometric Bead Array (CBA) inflammation kit for quantitative determination of cytokines IL-10, TNF, IL-1, IL-6 and IL-8. Shown are concentrations measured in individual samples after dilution. None of the nanoparticle formulations resulted in cytokine induction.

Cytokine Secretion by PBMC (ITA-10)

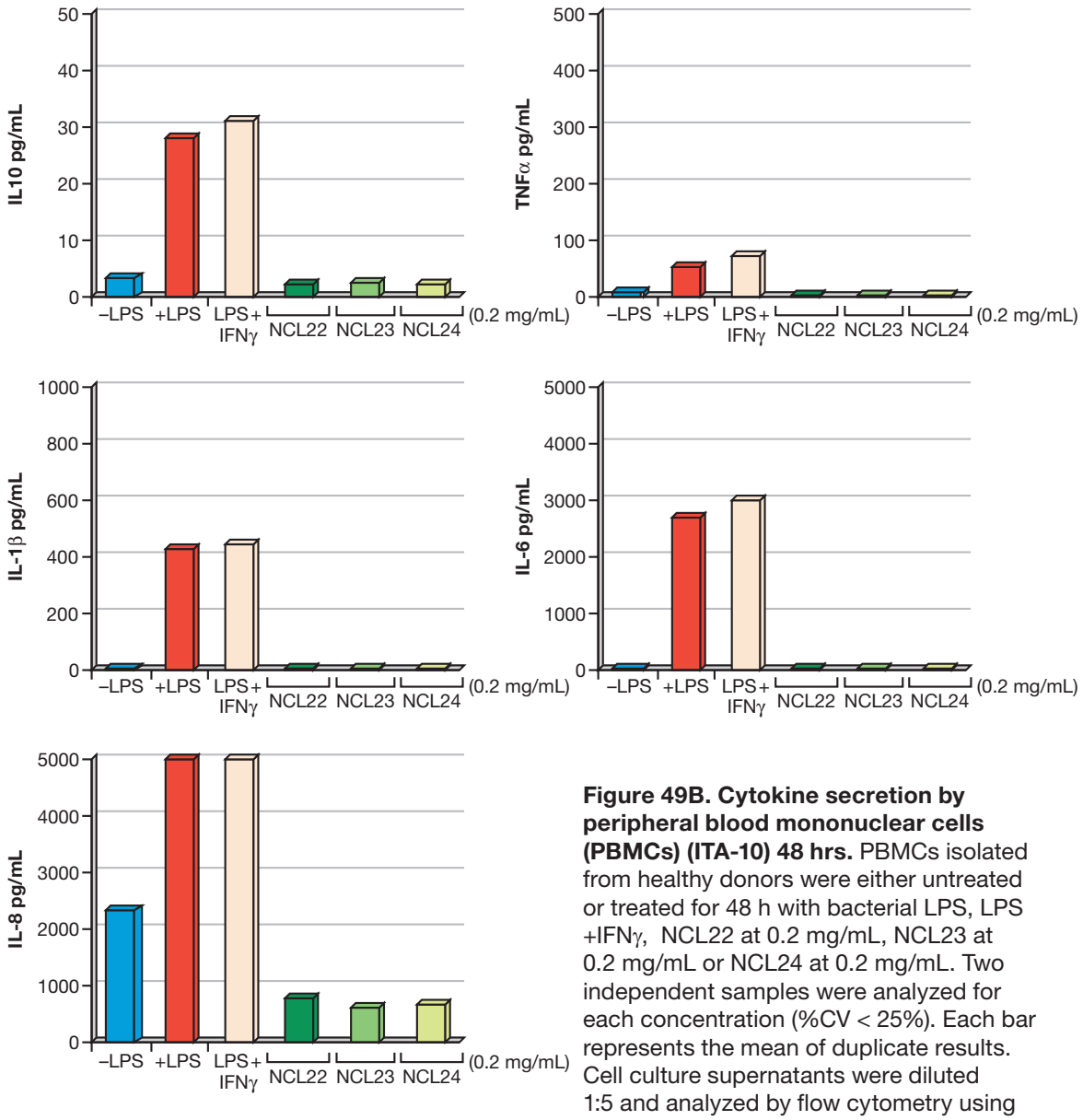

Figure 49B. Cytokine secretion by peripheral blood mononuclear cells (PBMCs) (ITA-10) 48 hrs. PBMCs isolated from healthy donors were either untreated or treated for 48 h with bacterial LPS, LPS +IFNγ, NCL22 at 0.2 mg/mL, NCL23 at 0.2 mg/mL or NCL24 at 0.2 mg/mL. Two independent samples were analyzed for each concentration (%CV < 25%). Each bar represents the mean of duplicate results. Cell culture supernatants were diluted 1:5 and analyzed by flow cytometry using a CBA inflammation kit for quantitative determination of cytokines IL-10, TNF, IL-1, IL-6 and IL-8. Shown are concentrations measured in individual samples after dilution. None of the nanoparticle formulations resulted in cytokine induction.

Potential NCL22 Effects on LPS-Induced Cytokine Secretion by PBMC (ITA-10)

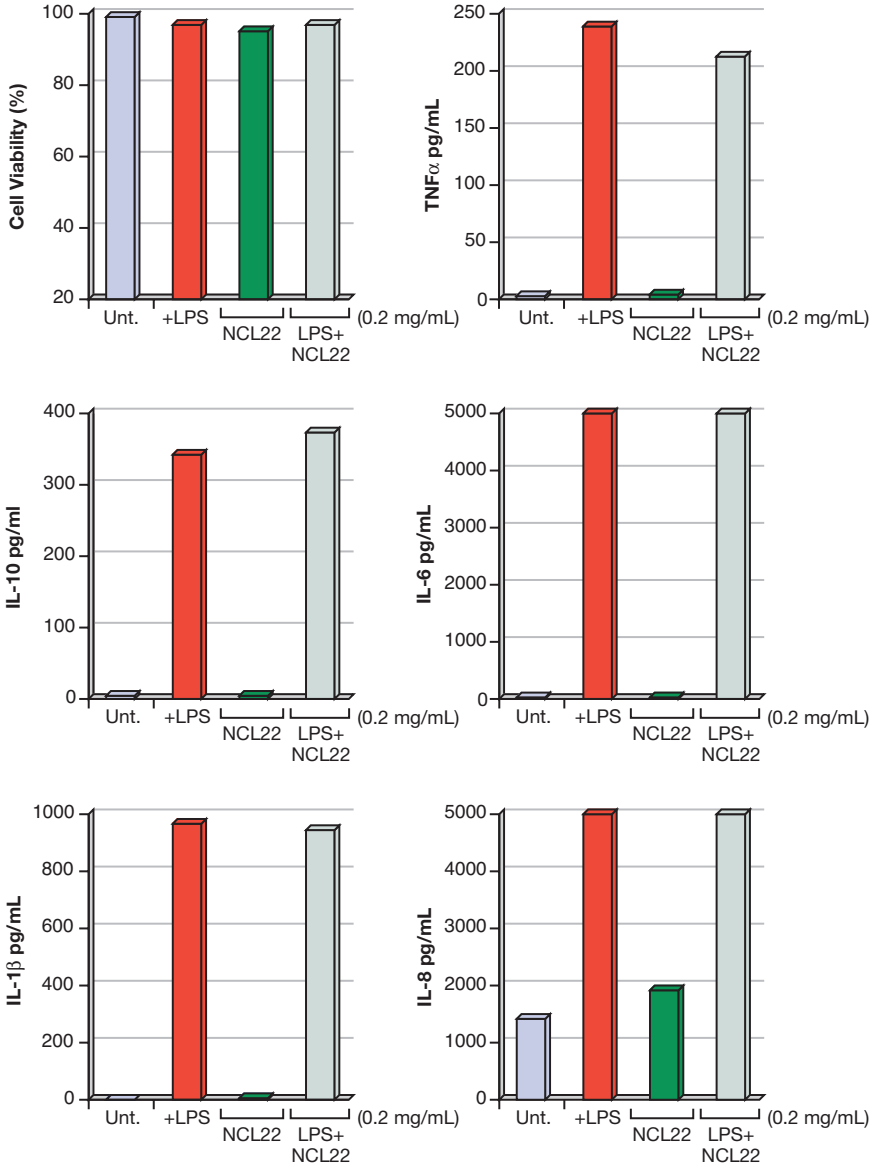

Figure 49C. Analysis of potential effects of NCL22 on LPS-induced cytokine secretion by peripheral blood mononuclear cells (PBMCs) (ITA-10). PBMCs isolated from healthy donors were either untreated (#1) or treated for 24 h with bacterial LPS (#2), NCL22 at 0.2 mg/mL(#3), LPS and NCL22 at 0.2 mg/mL (#4). Two independent samples were analyzed for each concentration (%CV < 25%). Each bar represents the mean of duplicate results. Viability of the cells was evaluated by trypan blue exclusion assay at the end of the 24 hour incubation. Cell culture supernatants were diluted 1:5 and analyzed by flow cytometry using a CBA inflammation kit for quantitative determination of cytokines IL-10, TNF, IL-1, IL-6 and IL-8. Shown is the mean concentration of cytokine in two independent samples after dilution. CV is less than 25%, except for NCL22 in the IL-6 and IL-8 plots, where CV is less than 50%. The tested formulation did not suppress LPS-induced cytokine production by PBMCs.

Cytotoxic Activity of NK Cells by ^{51}Cr-release Assay (ITA-11A)

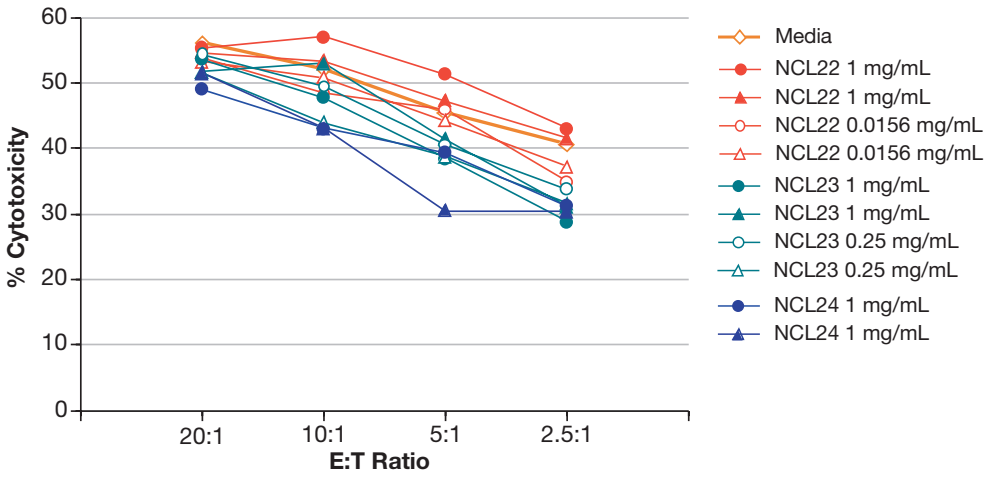

Figure 50A. Analysis of cytotoxic activity of NK cells by ^{51}Cr-release Assay (ITA-11A). The NK cell line NK92 (source Laboratory of Experimental Immunology [LEI]) and tumor cell line K562 (source Developmental Therapeutics Program [DTP]) were used as effectors and targets, respectively. The effector and 51Cr-loaded target cells were co-cultured at different effector-to-target (E:T) ratios without, or in the presence of, NCL22, NCL23, and NCL24. For each concentration, two independent samples were prepared and analyzed in triplicate (%CV < 20%). Each data point represents the mean of triplicate results. Additional samples were included to control for nanoparticle-induced chromium release from target cells. NCL22 at both concentrations and NCL23 at a low concentration did not interfere with the cytotoxicity of NK cells, while high doses of NCL23 and NCL24 slightly inhibited the cytotoxicity of NK cells towards K562 targets.

Cytotoxic Activity of NK Cells by Real-Time Cell Electronic Sensing (RT-CES)

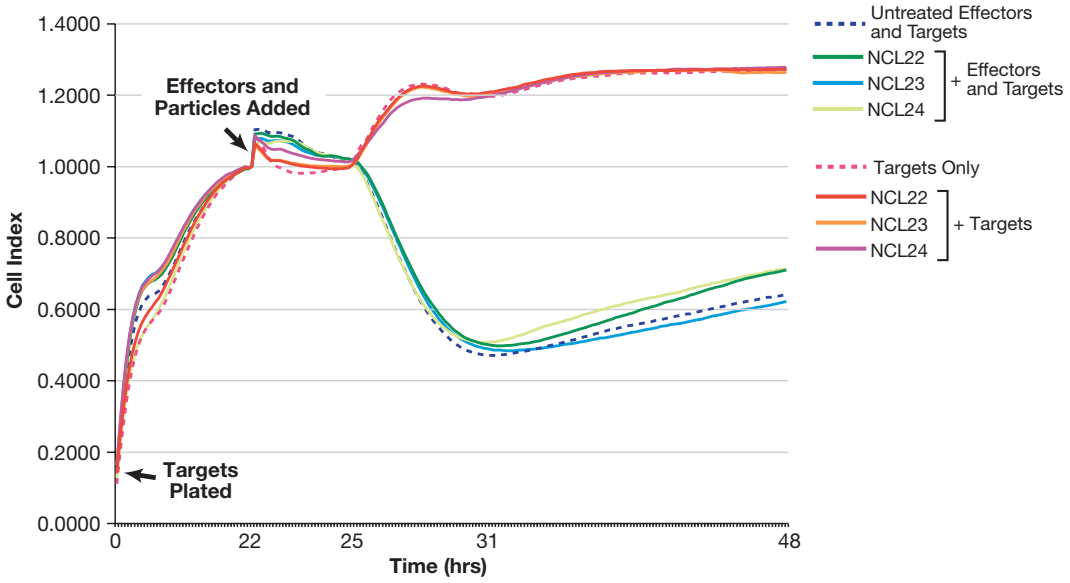

Figure 50B. Analysis of cytotoxic activity of NK cells by (RT-CES). The NK cell line NK92 (source American Type Culture Collection [ATCC]) and tumor cell line HepG2 (source DTP) were used as effectors and targets, respectively. Effector and target cells were co-cultured at an effector-to-target (E:T) ratio of 1:5 without, or in the presence of, NCL22, NCL23, and NCL24 (%CV < 20%). Additional samples were included to control for nanoparticle-associated toxicity to target cells. Cell viability was continuously monitored in real time for 48 h. Data were collected every 30 min during the first 22 h, every 2 min from 22 to 25 h, and every 10 min from 26 to 48 h. Nanoparticles did not interfere with the instrument detection system and were not toxic to tumor targets. NCL22, NCL23, and NCL24 did not interfere with cytotoxicity of NK cells towards tumor targets. NCL22 and NCL24 slightly inhibited the viability of effector NK92 cells.

Cytotoxic Activity of NK Cells by RT-CES

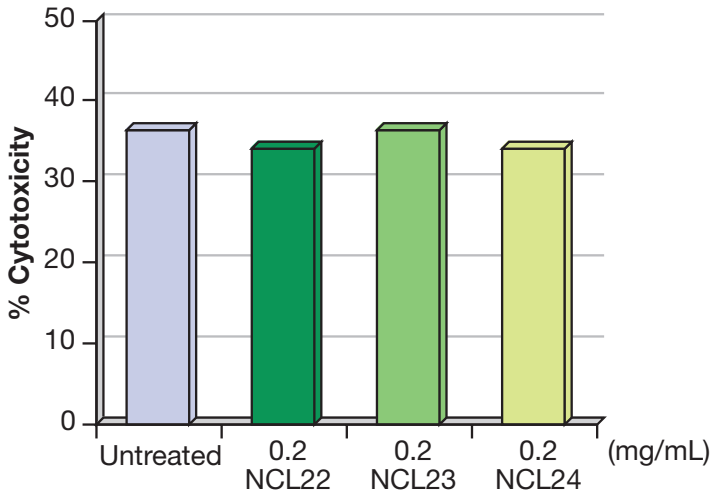

Figure 50C. Analysis of cytotoxic activity of NK cells by RT-CES. The NK cell line NK92 (source ATCC) and tumor cell line HepG2 (source DTP) were used as effectors and targets, respectively. The effector and target cells were co-cultured at an effector-to-target (E:T) ratio of 1:5 untreated or in the presence of NCL22, NCL23, or NCL24 at a concentration of 0.2 mg/mL. Cell viability was continuously monitored in real time for 48 h. The percentage of cytotoxicity was calculated by comparing the AUC values of untreated cells or of cells co-cultured in the presence of nanoparticles with that of the target's growth curve. Results from duplicate samples are shown (%CV < 20%). Each bar represents the mean of duplicate results. NCL22, NCL23, and NCL24 did not interfere with the cytotoxicity of NK cells towards tumor targets.

CONTRIBUTORS

Nanotechnology Characterization Laboratory Staff:

Scott E. McNeil, Ph.D., Director

Anil K. Patri, Ph.D., Senior Scientist

Steve Stern, Ph.D., Scientist

Marina Dobrovolskaia, Ph.D., Scientist

Jiwen Zheng, Ph.D., Scientist

Jeffrey Clogston, Ph.D., Scientist

Banu S. Zolnik, Ph.D., Postdoctoral Fellow

Chris McLeland, Senior Research Associate

Timothy M. Potter, Research Associate

Barry W. Neun, Research Assistant

Sarah Skoczen, M.S., Research Assistant

—

Dr. Vincent A. Hackley (NIST)

Dr. Gregory C. Turk (NIST)

Anna Mason (NCI)

Marcelino Bernardo, M.S. (SAIC-Frederick, Inc.)

ABBREVIATIONS

2D PAGE	Two-Dimensional Polyacrylamide gel Electrophoresis
^{51}Cr	51 Chromium
ABN	Abnormal Plasma Standard
AFFF	Asymmetrical Field Force Fractionation
APTT	Activated Partial Thromboplastin Time
ATCC	American Type Culture Collection
AUC	Area Under the Curve
CBA	Cytometric Bead Array
CE	Capillary Electrophoresis
CFU-GM	Colony Forming Units-Granulocyte Macrophage
CV	Coefficient of Variation
CVF	Cobra Venom Factor
DAB	DiaminoButane
DHB	2,5-dihydroxybenzoic acid
DI (H2O)	Deionized H2O
DLS	Dynamic Light Scattering
dn/dc	Differential Index of Refraction
DNT	Dendritic Nanotechnologies, Inc.
DTP	Developmental Therapeutics Program
E:T ratio	Effector: Target Ratio
ELISA	Enzyme-Linked Immunosorbent Assay
FBS	Fetal Bovine Serum
FDA	Food and Drug Administration
Gd-DTPA (Magnevist®)	Gadopentetate Dimeglumine
HEP-G2	Human Hepatocarcinoma Cells
HPLC	High Performance Liquid Chromatography
ICP-EOS	Inductively Coupled Plasma Optical Emission Spectroscopy
IL	Interleukin
K562	Human Erythroleukemia Cell Line
kDa	Kilodalton
kV	Kilovolt
LAL	Limulus Activation Lysate
LDH	Lactate Dehydrogenase
LEI	Laboratory of Experimental Immunology

LLC-PK1	Porcine Renal Proximal Tubule Cells
LPS	Lipopolysaccharide
MALDI-TOF	Matrix Assisted Laser Desorption/Ionization – Time of Flight
MALLS	Multiple Angle Light Scattering
mg	Milligram
mL	Milliliter
mm	Millimeter
MRI	Magnetic Resonance Imaging
MS	Mass Spectroscopy
MTT	3-(4,5-dimethyl-2-thiazolyl)-2,5-diphenyl-2H-tetrazolium bromide
N	Normal plasma standard
NCL	Nanotechnology Characterization Laboratory
NIST	National Institute of Standards and Technology
NNLS	Non Negative Least Square
nm	Nanometer
NO	Nitrous Oxide
PAMAM	Poly(amidoamine)
PBMC	Peripheral Blood Mononuclear Cells
PBS	Phosphate Buffered Saline
PHA-M	Phytohemaglutinin-M
psi	Pounds per Square Inch
PT	Prothrombin Time
RDG	Rayleigh-Debye- Gans
RAW 264.7	Mouse Leukemic Macrophage Monocyte Cell Line
RT-CES	Real Time- Cell Electronic Sensing
SAIC	Science Applications International Corporation
SEC	Size Exclusion Chromatography
SPGR	Spoiled Gradient Echo Sequences
T1, T2	Longitudinal Relaxation, Latitudinal Relaxation
TNF	Tumor Necrosis Factor
Unt	Untreated
UV-Vis	Ultra Violet- Visible
v/v	volume/volume